UNIVERSITY OF COPENHAGEN
FACULTY OF SCIENCE
NIELS BOHR INSTITUTE

Master's Thesis

Falk Marius Oraschewski btv655@alumni.ku.dk

Modelling of firn densification in the presence of horizontal strain rates

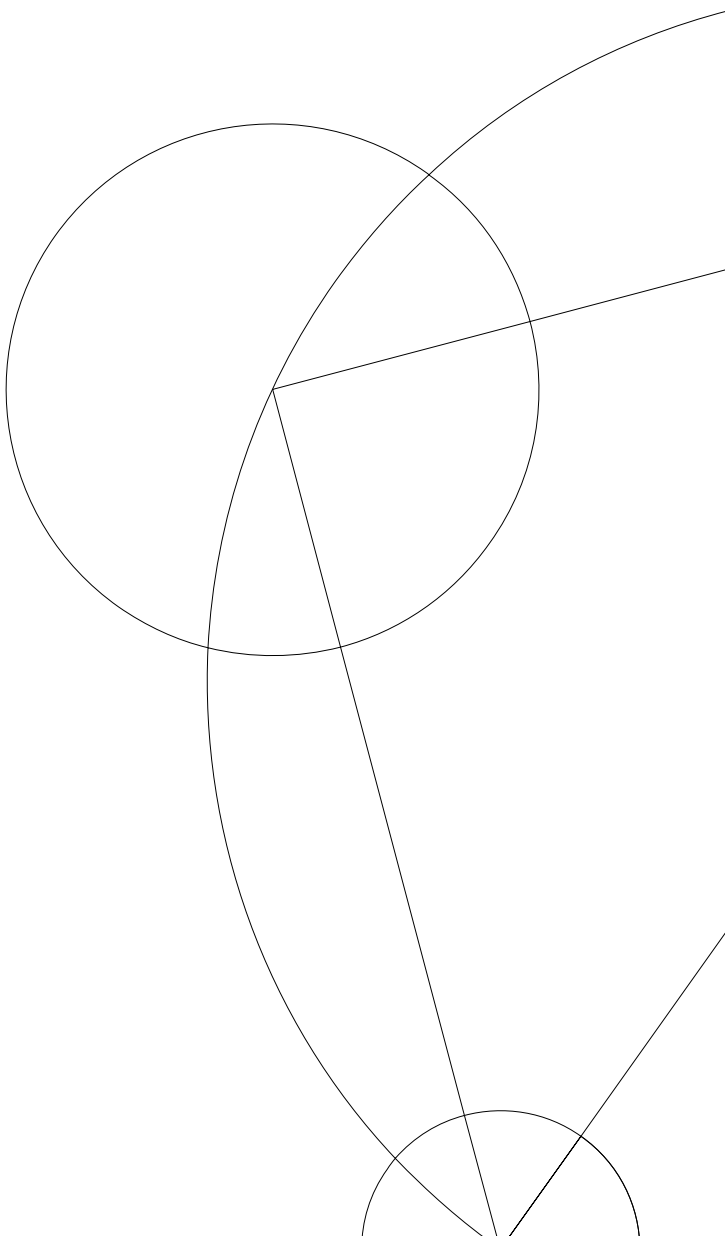

Supervisor: Aslak Grinsted

5th September 2020

Abstract

The densification of polar firn that is subjected to horizontal strain rates is studied. A model for the enhanced densification of the firn by strain softening is developed. Strain softening describes an acceleration of power-law creep in the presence of high horizontal strain rates, which was suggested to explain the occurrence of exceptionally thin firn in the shear margins of ice streams. With the model the effect of strain softening is compared to other strain-driven densification mechanisms, like pure shear and strain heating, and to potential variations of temperature and accumulation rate. Thereby, strain softening is identified to dominate firn densification at high strain rates. A recorded density profile along a cross-section of the North-East Greenland ice stream (NEGIS) is reproduced with the presented model with good agreement in the shear margins. There, the thinning of the firn correlates with the location and magnitude of the shear margin troughs, which indicates that their formation is caused by strain softening. In regions with low strain rates the model overestimates the densification rate. Because of a particularly strong sensitivity of the model to low strain rates and the presence of non-zero strain rates on large parts of the Greenland Ice Sheet (GrIS), it is suggested that empirically tuned densification models already implicitly consider moderate horizontal strain rates. Besides the temperature and the accumulation rate, the effective horizontal strain rate is therefore proposed as a third forcing parameter, that needs to be considered in the development of a physics-based firn densification model.

Acknowledgement

First of all, I would like to deeply thank my supervisor Aslak Grinsted for bringing this interesting topic to my attention and for having an open door and offering good advice, whenever I felt to be stuck on the way. I moreover would like to thank Sebastian B. Simonsen for agreeing to examine this thesis.

Moreover, I am grateful to Iben Koldtoft for dedicatedly helping me to find firn cores for the validation of my model, Helle A. Kjær and Paul T. Vallelonga for providing me with the firn core data and David A. Lilien for sharing with me the preprocessed radar data and tools to easily work with them. I also acknowledge Ruth Mottram and the Arctic and Climate Research section at the Danish Meteorological Institute for producing and making available their HIRHAM5 model output and Kiya Riverman et al. for sharing the data of their seismic survey in the NEGIS region. This help enabled me to look at firn densification from such diverse perspectives.

I further want to thank Christine S. Hvidberg for fruitful discussions on firn modelling and Ralf Greve for giving advise on the regularisation of the model. I acknowledge Ann-Sofie Priergaard Zinck and Marco Hoffmann for giving very useful feedback on the appearance of the thesis and correctness of the mathematical formulations.

Finally, I would particularly like to thank Janina, for encouraging me in the last month of the thesis, when the deadline was approaching, and my family for supporting me during my studies and enabling me to find my own way. Without this freedom, I would not have ended up in the amazing field of glaciology.

Corrected edition

The first edition of this Master's thesis was submitted on 17 August 2020.
In this edition some typing errors have been corrected.

Contents

1. Introduction

Firn densification is one of the most fundamental processes in glaciology as it describes how the matter of all studies, the ice, is being formed. The existence of the Greenland and Antarctic Ice Sheets (GrIS and AIS), which cover the major landmasses in Earth's polar regions, is ensured by a gradual supply of fresh snow, which accumulates over time, because it does not melt in the central parts of the ice sheets, thanks to the low solar irradiance in high latitudes, the high elevation of the ice sheet surfaces and the high albedo of snow itself. As the supply comes in the form of snow, it must undergo a transformation into the glacial ice that can be observed in ice cores or at the outlet glaciers.

Initially, the fresh snow is very loose and can get drifted away by the wind, but with time it settles and eventually gets buried under younger snow. At this stage the old snow has formed into a porous medium, which is called *firn*. The firn is compressed under the weight of the younger snow and thereby gets gradually compacted. This process is accordingly called *firn densification*. Despite its fundamental character and its importance for the interpretation of many glaciological observations, firn densification is not well understood and no generally accepted physically-based model of firn densification exists. This is caused by the fact, that the firn does not densify by a single, but by a multitude of different microscale processes that are dominant at different densities, respectively depths, and jointly contribute to a variable densification rate. Attempts to model the individual processes were made (Alley, 1987; Arnaud et al., 2000), but for practical applications strongly parametrised, empirical models like the Herron-Langway model (Herron and Langway,

1980) are still widely used.

The aim of this study is to better understand firn densification in the presence of horizontal strains, because classical models in general only consider the temperature and accumulation rate as forcing parameters, even though a lower firn thickness and hence an enhanced firn densification rate was observed in the shear margins of ice streams, where horizontal strain rates are high. These observations suggested that the compaction by power-law creep is increased due to the effect of strain softening, which describes a strain-induced reduction of the viscosity (Alley and Bentley, 1988; Riverman et al., 2019). In this thesis the effect of strain softening on the densification rate is modelled for the first time and compared to other potential densification mechanisms that can affect firn densification in the shear margins of an ice stream.

The model can thereby contribute to a better understanding of the dynamics of ice streams, which is needed, in order to assess their stability under changing climatic conditions for the estimation of their potential contribution to future sea-level change (e.g. Christianson et al., 2014). To answer this question, since 2016 a deep ice core is being drilled in the centre of the North-East Greenland Ice Stream (NEGIS) in the scope of the East Greenland Ice-Core Project (EGRIP) (Vallelonga et al., 2014; Mojtabavi et al., 2019), which is accompanied by several associated projects, involving for example the GPS mapping of surface velocity and ground-based and airborne radar surveys of the ice sheet and the firn. Of particular interest for this thesis are the firn cores that have been drilled in NEGIS and its shear margins and a density profile, which was inferred from seismic velocities that were recorded along a cross-section of NEGIS by Riverman et al. (2019). On one hand, these diverse projects provide data that can be used to assess the impact of firn densification by horizontal strain rates, but on the other hand, the developed model can also support the interpretation of these observations.

Besides these direct applications, the study contributes to a better understanding of firn densification itself by generally assessing the im-

portance of horizontal strain rates on the densification process. The thesis moreover makes a contribution to the development of a physically-based densification model, by presenting a model for the process of strain softening, which can easily be included as an extension to any other firn densification model.

2. Theoretical background

In this thesis the influence of large scale glacier dynamics via horizontal strain rates on the local densification of firn is studied. Therefore, the concepts of stress, strain and strain rate are detailed first, based on Cuffey and Paterson (2010, App. A) with additions from Lautrup (2011) and van der Veen (2013). Subsequently, a constitutive equation for the rheology of ice is described, which gives the relation between stress and strain rate. In the last part, the dominant firn densification mechanisms and important characteristics of the firn are discussed.

In the following, a Cartesian coordinate system is used, where the x- and y-directions can be interpreted as pointing eastwards and northwards, respectively. The z-direction represents the depth and is pointing vertically downwards.

2.1. Stress, strain and strain rates

2.1.1. Stress

The structure of the firn is stabilised by forces acting between neighbouring grains. When looking at the medium as a whole, the state of these internal forces is typically described with a quantity called *stress*, defined as force per unit area. Thus, the stress acting on one side of some interface must be balanced by a counteracting stress on the opposite side and like the force, the stress is a vector quantity.

The stress component σ_{ij} at a point P that is induced by a force $\delta\mathbf{F}$ in i-direction on an infinitesimal area δA_j with the normal vector pointing

in j-direction is given by

$$\sigma_{ij} = \frac{\delta \mathbf{F}_i}{\delta A_j}, \tag{2.1}$$

(Lautrup, 2011, Ch. 6).

For the area δA_z that lies in the xy-plane the normal is pointing in z-direction. Its component σ_{zz} that is parallel to the normal vector is called *normal stress*. By definition this normal stress can be understood as a *tensile stress*, when positive, and as a *compressive stress*, when it is negative. The components σ_{xz} and σ_{yz} that lie in the xy-plane, and hence are perpendicular to the normal vector, are called *shear stresses*.

The full state of stresses in the point P is described by the second-order *stress tensor*

$$\boldsymbol{\sigma} = \begin{pmatrix} \sigma_{xx} & \sigma_{xy} & \sigma_{xz} \\ \sigma_{yx} & \sigma_{yy} & \sigma_{yz} \\ \sigma_{zx} & \sigma_{zy} & \sigma_{zz} \end{pmatrix}, \tag{2.2}$$

where the components acting on the planes with normal vectors pointing in x- and y-direction can be derived similarly as explained above.

According to Eq. (2.2), nine components are in principle needed to describe the full state of stress at every point within a medium. However, when the system is in balance, as it generally is, the shear stress com-

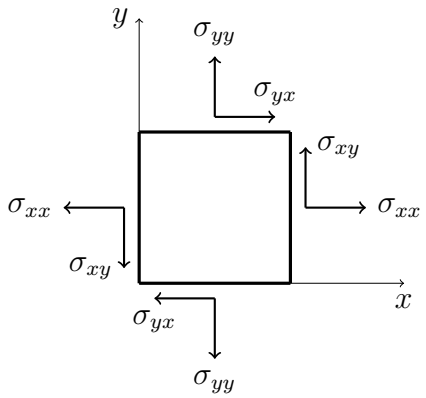

Figure 2.1.: Stress balance. Reconstructed from Cuffey and Paterson (Fig. A.2, 2010).

ponents in one plane that act on the sides of some parcel must be equal, as shown in Fig. 2.1. Otherwise the parcel would begin to rotate. Consequently, the stress tensor must be symmetric, with $\sigma_{xy} = \sigma_{yx}$, $\sigma_{xz} = \sigma_{zx}$ and $\sigma_{yz} = \sigma_{zy}$.

Under a Cartesian coordinate transformation the trace of the stress tensor

$$\mathrm{tr}(\boldsymbol{\sigma}) = \sigma_{xx} + \sigma_{yy} + \sigma_{zz} \tag{2.3}$$

is invariant. This is typically used to define the *pressure* as the negative of the mean of its components by

$$p = -\frac{1}{3}\left(\sigma_{xx} + \sigma_{yy} + \sigma_{zz}\right), \tag{2.4}$$

so that it is a compressive stress.

In the firn it can approximately be associated with the hydrostatic pressure

$$p(z) = g \int_z^{z_s} \rho(z')\,\mathrm{d}z'\,, \tag{2.5}$$

where g is the gravitational acceleration, ρ the density of the firn and z_s the surface height. In this context $-\sigma_{zz}$ is also defined as the load σ with

$$\sigma = p = -\sigma_{zz}. \tag{2.6}$$

Stress deviator

With the stress tensor and the pressure, we can further define the *stress deviator*. Its tensor is given by the traceless part of the stress tensor:

$$\boldsymbol{\tau} = \boldsymbol{\sigma} - \mathrm{tr}(\boldsymbol{\sigma})\mathbf{I} = \boldsymbol{\sigma} + p\mathbf{I}. \tag{2.7}$$

As a consequence, the shear components of stress and stress deviator are identical, while the trace of the stress deviator vanishes:

$$\mathrm{tr}(\boldsymbol{\tau}) = \tau_{xx} + \tau_{yy} + \tau_{zz} = 0. \tag{2.8}$$

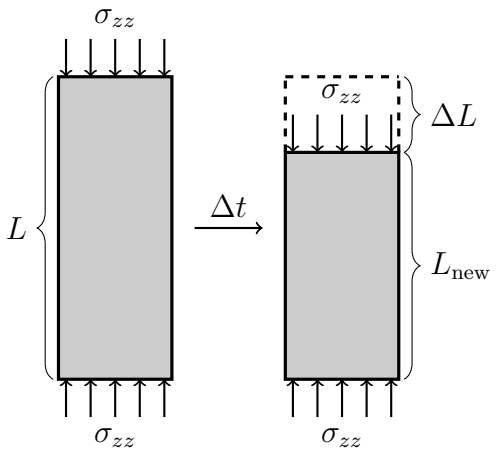

Figure 2.2.: Normal strain in vertical direction.

2.1.2. Strain

External stress induces a deformation of the firn. The strength of this deformation in a medium with respect to some reference state can be measured as *strain*. It is a description of how the geometry of some parcel in this medium has changed within an external coordinate system. Again, one can distinguish between normal and shear strain.

Normal strain indicates the change of the distance between two points along a corresponding coordinate axis. This can be illustrated by the example of some firn column, where the upper and lower edge are marked by distinct layers with a vertical distance of L. When looking at the firn column after some time, it will have become compressed under the load $\sigma_z z$ of the younger snow and the distance between the two layers will have decreased by some length $\Delta L = L_{\text{new}} - L$, as displayed in Fig. 2.2. The strain in vertical direction is then given by

$$\varepsilon_{zz} = \frac{\Delta L}{L}. \tag{2.9}$$

Accordingly, the strain induced by a negative, compressive stress is negative, as well, and for a tensile stress it is positive. Equation (2.9) further

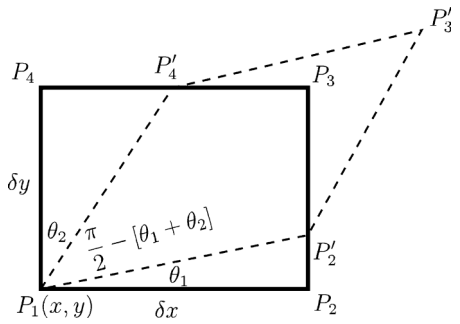

Figure 2.3.: The effect of shear strain. Adopted from Cuffey and Paterson (Fig. A.6, 2010).

shows that strain is a dimensionless quantity, meaning that it describes the relative change of the displacement.

Shear strain on the other hand refers to a change of the angular orientation of the connecting line between two points in the external coordinate system. Thus, it describes how an extended element in a medium under shear stress changed its angular shape and rotated between the initial and final state, see Fig. 2.3. In this example, the shear strain can be computed by

$$\varepsilon_{xz} = \frac{\theta_1 + \theta_2}{2}. \tag{2.10}$$

2.1.3. Strain rate

Because the strain is a dimensionless quantity that only tells something about the deformation in a medium between two arbitrary states, it is not a practical quantity to use for explaining physical processes and for comparing different observations. Therefore, *strain rates* are introduced as strain per time. For the example of the normal strain in Eq. (2.9) it is given by

$$\dot{\varepsilon}_{zz} = \lim_{\Delta t \to 0} \frac{\varepsilon_{zz}}{\Delta t} = \lim_{\Delta t \to 0} \frac{\Delta L}{L \Delta t} = \frac{1}{L} \frac{\mathrm{d}L}{\mathrm{d}t}, \tag{2.11}$$

where Δt is the time between the initial and final state.

Strain rate tensor

As strains, respectively strain rates, are directly linked to stresses, also nine strain rates are needed at any poifnt in a medium to describe the full state of strain rates. These strain rates form the strain rate tensor

$$\dot{\boldsymbol{\varepsilon}} = \begin{pmatrix} \dot{\varepsilon}_{xx} & \dot{\varepsilon}_{xy} & \dot{\varepsilon}_{xz} \\ \dot{\varepsilon}_{yx} & \dot{\varepsilon}_{yy} & \dot{\varepsilon}_{yz} \\ \dot{\varepsilon}_{zx} & \dot{\varepsilon}_{zy} & \dot{\varepsilon}_{zz} \end{pmatrix}. \tag{2.12}$$

When the velocity field in the medium is known, its components can be computed by

$$\dot{\varepsilon}_{ij} = \frac{1}{2}\left(\frac{\partial u_i}{\partial x_j} + \frac{\partial u_j}{\partial x_i}\right), \tag{2.13}$$

where (u_x, u_y, u_z) are the components of the velocity field in the directions $(x_x, x_y, x_z) = (x, y, z)$. Accordingly, the strain rate tensor is also a symmetric second-order tensor.

Strain rate invariants

Such a tensor has three independent invariants, which do not change under a Cartesian coordinate transformation It can be shown that they are given by the following expressions. The first, is the trace, given by

$$\dot{\varepsilon}_{\mathrm{I}} = \mathrm{tr}(\dot{\boldsymbol{\varepsilon}}) = \dot{\varepsilon}_{xx} + \dot{\varepsilon}_{yy} + \dot{\varepsilon}_{zz}. \tag{2.14}$$

Similar expressions were introduced before in Eqs. (2.3) and (2.8) for the stress and the stress deviator. In an incompressible medium the trace of the strain rate vanishes ($\dot{\varepsilon}_{\mathrm{I}} = 0$), because the volume of any parcel in the medium cannot change.

The second invariant of the strain rate tensor is the square of the *effective strain rate* $\dot{\varepsilon}_{\mathrm{E}}$, defined by

$$\dot{\varepsilon}_{\mathrm{II}} = \dot{\varepsilon}_{\mathrm{E}}^2 = \frac{1}{2}\left[\dot{\varepsilon}_{xx}^2 + \dot{\varepsilon}_{yy}^2 + \dot{\varepsilon}_{zz}^2\right] + \dot{\varepsilon}_{xy}^2 + \dot{\varepsilon}_{xz}^2 + \dot{\varepsilon}_{yz}^2. \tag{2.15}$$

The effective strain rate can be understood as an additive measure of the magnitude of all strain rate components. Its equivalent for the stress deviator, the *effective stress* is defined analogously. The third invariant is the determinant of the strain rate tensor $\dot{\varepsilon}_{\mathrm{III}} = \det(\dot{\boldsymbol{\varepsilon}})$, which, however, does not have a direct meaning in glacier dynamics (van der Veen, 2013, Ch. 1).

Horizontal strain rate tensor

In this thesis the impact of the horizontal strain on firn densification is studied. Therefore, in some calculations only the horizontal strain rates that lie in the xy-plane are considered. In this case the strain rate tensor reduces to

$$\dot{\boldsymbol{\varepsilon}}_{\mathrm{H}} = \begin{pmatrix} \dot{\varepsilon}_{xx} & \dot{\varepsilon}_{xy} \\ \dot{\varepsilon}_{yx} & \dot{\varepsilon}_{yy} \end{pmatrix}. \tag{2.16}$$

It is also a second order tensor. Its first invariant can be determined by

$$\dot{\varepsilon}_{\mathrm{I,H}} = \dot{\varepsilon}_{xx} + \dot{\varepsilon}_{yy} \tag{2.17}$$

and the second invariant by

$$\dot{\varepsilon}_{\mathrm{II,H}} = \dot{\varepsilon}^2_{\mathrm{E,H}} = \frac{1}{2}\left[\dot{\varepsilon}^2_{xx} + \dot{\varepsilon}^2_{yy}\right] + \dot{\varepsilon}^2_{xy}, \tag{2.18}$$

which is denoted as the square of the *effective horizontal strain rate*.

These invariants are in accordance with those of the three-dimensional tensor in Eqs. (2.14) and (2.15), when the vertical and antiplane components (with $i = z$ or $j = z$) are neglected. Hence, they can be understood as the horizontal contributions to the invariants of the full strain rate tensor.

Principle axes of strain rate

It can be shown, that a symmetric second-order tensor is diagonalisable, meaning that it can be transformed such, that it only contains normal

components. These normal components are the eigenvalues of the tensor (Lautrup, 2011, Ch. 7). For the horizontal strain rate tensor they can be calculated by

$$\begin{aligned} \dot{\varepsilon}_1 &= \frac{1}{2}\left(\mathrm{tr}(\dot{\varepsilon}_\mathrm{H}) + \sqrt{\mathrm{tr}(\dot{\varepsilon}_\mathrm{H})^2 - 4\det(\dot{\varepsilon}_\mathrm{H})}\right) \\ \dot{\varepsilon}_2 &= \frac{1}{2}\left(\mathrm{tr}(\dot{\varepsilon}_\mathrm{H}) - \sqrt{\mathrm{tr}(\dot{\varepsilon}_\mathrm{H})^2 - 4\det(\dot{\varepsilon}_\mathrm{H})}\right) \end{aligned} \tag{2.19}$$

and are denoted as *principal strain rates*. They act along the *principal axes of strain rates*, which are the corresponding eigenvectors. Because ice sheets are flat, the flow of the ice in horizontal direction is generally much faster than in vertical direction. Thus, the horizontal components of the strain rate are in general also much bigger than the vertical and it follows with Eqs. (2.14) and (2.19) that the first principal strain rate is typically positive and tensile, while the second is negative and compressive.

When the principle strain rates are used, the effective horizontal strain rate can be written in the short form of

$$\dot{\varepsilon}_{\mathrm{E,H}} = \sqrt{\frac{1}{2}\left[\dot{\varepsilon}_1^2 + \dot{\varepsilon}_2^2\right]}, \tag{2.20}$$

because the shear strain rate components vanish in the coordinate system of the principle axes of strain rates.

2.2. Rheology of ice

As explained before, stress causes deformation and thus strain in a medium. The relation between the two quantities depends on the medium itself and is given by a constitutive relation, which describes the rheology of the medium. When firn or ice is subjected to external stress, it deforms slowly and steadily. This behaviour is called creep and the constitutive relation is hence termed a creep relation.

2.2.1. Glen's flow law

The most established creep relation for ice is *Glen's flow law* (Glen, 1955). It was empirically derived in laboratory experiments for the stress range relevant for glacial flow, but could also demonstrate its applicability in field observations. It states that the dominant stress deviator induces a strain rate that is given by a power law:

$$\dot{\varepsilon} = A\tau^n. \tag{2.21}$$

In this equation A is called the *creep parameter*. It describes how the properties of the ice, like the temperature or the ice fabric, affect its rheology. The effect of the temperature is generally assumed to be dominant, so that the creep parameter is typically given by an Arrhenius-type temperature equation.

The second variable in Eq. (2.21) is the *creep exponent* n. In the case of $n = 1$ the strain rate is directly proportional to the stress, which is termed a Newtonian viscous behaviour. In a wide range of studies the dynamics of ice could be represented best with a value of $n = 3$. This means that ice in general behaves like a Non-Newtonian fluid. However, the creep exponent can vary between different creep mechanisms, so that under certain conditions other values of the creep exponent in the range of $n = 1$ to 4 were suggested (Cuffey and Paterson, 2010, Ch. 3).

Nye's generalisation of Glen's flow law

Glen's Flow law was generalised by Nye (1957) for cases with a more complex arrangement of stresses, by postulating that the effective stress and the effective strain rate, which are measures for the overall state of stress, respectively strain rate, must follow the same relationship as the dominant components in Glen's flow law (2.21):

$$\dot{\varepsilon}_{\mathrm{E}} = A\tau_{\mathrm{E}}^n. \tag{2.22}$$

Nye moreover assumes that the ice is isotropic and that each strain component is proportional to its corresponding stress component with a proportionality constant λ, which, accordingly, does not depend on the coordinate system and is the same for all components:

$$\dot{\varepsilon}_{ij} = \lambda \tau_{ij}. \tag{2.23}$$

The constant of proportionality λ represents the fluidity of the ice, which is the reciprocal of the viscosity. Considering the characteristic property of the stress deviator, that its trace is disappearing, see Eq. (2.8), the proportionality relation also implies incompressibility.

Because the effective stress is defined analogously to the effective strain rate, see Eq. (2.15), it follows from Eq. (2.23) that

$$\dot{\varepsilon}_{\mathrm{E}} = \lambda \tau_{\mathrm{E}} \tag{2.24}$$

and with Eq. (2.22) further that λ is given by

$$\lambda = A \tau_{\mathrm{E}}^{n-1}. \tag{2.25}$$

Inserting the proportionality factor back in Eq. (2.23) gives the *generalised Glen's Flow Law*:

$$\dot{\varepsilon}_{ij} = A \tau_{\mathrm{E}}^{n-1} \tau_{ij}. \tag{2.26}$$

2.2.2. Effective viscosity

Because with Eq. (2.13) strain rates can be measured significantly easier than stresses, a similar expression as Eq. (2.26) involving the effective strain rate is more practical for most applications. Equation (2.22) can be rewritten as

$$\dot{\varepsilon}_{\mathrm{E}}^{1/n-1} \dot{\varepsilon}_{\mathrm{E}} = A^{1/n} \tau_{\mathrm{E}}, \tag{2.27}$$

so that generalised Glen's Flow Law (2.26) with the effective strain rate is given by

$$\dot{\varepsilon}_{ij} = A^{1/n} \dot{\varepsilon}_{\mathrm{E}}^{m} \tau_{ij}, \tag{2.28}$$

with the exponent $m = 1 - 1/n$. Note that m is defined such that $m \geq 0$.

Because the constant of proportionality in Eq. (2.23) represents the fluidity, the *effective viscosity* of the ice can be defined by $\eta = 1/(2\lambda)$, such that

$$\dot{\varepsilon}_{ij} = \frac{1}{2\eta} \tau_{ij}. \tag{2.29}$$

With Eq. (2.28) it follows that the effective viscosity is given by

$$\eta = \left[2A^{1/n} \dot{\varepsilon}_{\mathrm{E}}^{m} \right]^{-1}. \tag{2.30}$$

When the ice behaves like a Newtonian viscous fluid with $n = 1$, then $m = 0$ and the strain rate, respectively stress, does not affect the viscosity. Ice, however, behaves in many situations like a Non-Newtonian fluid with $n = 3$. In this case, $m = 2/3$ follows and according to Eq. (2.30) the viscosity decreases with the effective strain rate. This means that strain, respectively the causal stress, induces a softening of the ice (Cuffey and Paterson, 2010, Ch. 3).

2.3. Firn densification

In the accumulation zones of ice sheets and mountain glaciers the temperatures are in general always below the melting point. Hence, precipitation solely occurs in the form of snow which does not melt over summer and gets buried under younger snow in the following years. Under the weight of the overlying snow it gradually transforms from old snow, with a density of around $315\,\mathrm{kg\,m^{-3}}$ (Fausto et al., 2018), into glacial ice, with a density of $917\,\mathrm{kg\,m^{-3}}$. During the transformation, the buried snow is called firn. In this stage it is a porous material, composed of bonded snow grains, where the pores are filled with air.

2.3.1. Densification mechanisms

The process of the transformation from snow to ice is called *firn densification*. The term, however, does not describe a single mechanism, but comprises a series of mechanisms, with varying densification rates, that are relevant in different density regimes (Maeno and Ebinuma, 1983). The corresponding changes of the densification rate can be observed in the density profiles of firn cores. To account for these changes, one typically distinguishes between three stages of firn densification.

First stage

The first stage corresponds to firn with a density of less than the *critical density* of $550\,\mathrm{kg\,m^{-3}}$, which can typically be observed in the upper 10 to 25 meters of the firn column. The dominant densification process in this stage is the Newtonian viscous *grain-boundary sliding* with an activation energy of $42\,\mathrm{kJ\,mol^{-1}}$. In this stage it proceeds significantly faster than other processes, that potentially are active at the same time. As the snow grains are very loosely packed in the beginning, the coordination number, that is the number of bonds per grain, has only a value of about two. Under the load the grains can thus slide along their boundaries into an optimised, densely packed position. Thereby, the coordination number increases gradually, until it approaches a value of six at the critical density. At this point the process ceases to be dominant, because on average each grain is hold in position by three others and most of the grains cannot move further (Alley, 1987).

Second stage

Subsequently, the densification of the firn by *pressure sintering* becomes important. This term refers to the formation and growth of necks at the bonds between neighbouring grains under external pressure, while the material is at high homologous temperature, i.e. the temperature is

relatively close to the melting point. Again, several pressure sintering mechanisms exist and act in parallel, which can be studied with the help of pressure sintering mechanism maps, that based on models for each mechanism show the dominant processes for certain configurations of temperature, density and pressure.

In such studies, *power-law creep*, also called dislocation creep, with an activation energy of $60\,\mathrm{kJ\,mol^{-1}}$ was found to be the dominant mechanism for the pressure sintering of firn at moderate temperatures and over large parts of the density range (Wilkinson, 1988; Maeno and Ebinuma, 1983). Thus, it is also considered to be the dominant densification mechanism in the second firn stage. This process corresponds to the plastic deformation of the firn and accordingly is given by a power-law expression similar to Glen's flow law (2.21):

$$\dot{\varepsilon}_{zz} = -A\sigma^n. \tag{2.31}$$

In this case, the strain rate depends on the load σ. Again, the creep parameter A primarily describes the influence of the temperature on the fluidity of the firn and the creep exponent is given by $n = 3$ (Ebinuma and Maeno, 1987). With similar arguments as made in the derivation of Eq. (2.29) it follows that

$$\dot{\varepsilon}_{zz} = -\frac{1}{2\eta}\sigma, \tag{2.32}$$

which means that the densification rate by power-law creep is inversely proportional to the viscosity which scales with the effective strain rate, as given in Eq. (2.30). Alley and Bentley (1988) have observed and suggested first, that in this way horizontal stresses, respectively strain rates, can accelerate the firn densification by power-law creep.

Ebinuma and Maeno (1987) identified a second transition of the densification rate at a density of around $700\,\mathrm{kg\,m^{-3}}$, when optimal packing of the snow grains is achieved, so that particle rearrangement terminates completely and power-law creep remains the only significant mechanism. In this interpretation grain-boundary sliding still contributes consider-

ably to firn densification between 550 and 700 $\mathrm{kg\,m^{-3}}$. Nevertheless, the bend in the density profiles at the optimal packing density is less pronounced at many sites, because power-law creep is already the dominant mechanisms before. Hence, this stage is generally not considered separately.

Third stage

Between densities of 800 and 830 $\mathrm{kg\,m^{-3}}$ the pores in the firn are gradually closed off and the remaining air gets trapped inside (Schwander et al., 1997), which is often considered as the firn-ice transition. Beyond this point the bubbly ice densifies further until the enclosed air has diffused into the ice lattice. In this final stage the densification rate by power-law creep is reduced, as the pressure in the bubbles rises, when the enclosed air gets compressed (Salamatin et al., 1997).

Other relevant densification mechanisms

Besides the above-mentioned processes, other mechanisms become significant under certain conditions.

Li and Zwally (2004) have discussed the importance of vapour transport in the upper firn stage at low temperatures, as observed especially on the Antarctic ice sheet. Driven by large temperature gradients in the firn due to the strong seasonal variability of the surface temperature, the densification rate is strongly affected by vapour transport within the firn. Low accumulation rates increase the importance of this effect further, because in this case a specific firn layer remains longer at shallow depth and is subjected to it for more years.

In the second, other pressure sintering processes such as lattice diffusion and grain boundary diffusion, which transport mass from the grain boundaries into the pores, may become dominant at low temperatures, as they have a lower activation energy than power-law creep (Wilkinson, 1988).

At locations with high temperatures on the other hand, melt occurs at the surface, which strongly affects the firn densification by the percolation and refreezing of meltwater and the formation of dense ice lenses within the firn (Braithwaite et al., 1994).

2.3.2. Transition between firn stages

The transitions between the different stages of firn densification were outlined above. However, at many locations the characteristic densities such as the critical density are shifted or no clear transition can be observed in the depth-density profile (Hörhold et al., 2011). This indicates that the transition between mechanisms is smoother than often assumed and that in certain density ranges multiple processes act together as discussed by Ebinuma and Maeno (1987).

For example at sites with low temperatures the transition between the first two stages was observed at a lower critical density. At such sites the densification proceeds slower and the load at the transition is higher. Although the activation energy of grain boundary sliding is lower than the one of power-law creep, the latter is increased at low temperatures, because it is a Non-Newtonian process with an exponent of $n = 3$ and gets accelerated by the additional load, while the Newtonian grain boundary sliding is not affected. In consequence, power-law creep becomes the dominant process earlier and the critical density is shifted towards lower values (Arnaud et al., 1998).

2.3.3. Important firn properties

In the following the most important properties of the firn column are briefly discussed.

Firn thickness

The density of $830\,\mathrm{kg\,m^{-3}}$ is defined as the *bubble close-off (BCO) density*. As it marks the transition from firn to ice, the corresponding *BCO depth* is considered as the thickness of the firn, which is typically on the order of 60 to 120 metres.

Age difference

Similarly, the BCO age is defined as the age of the firn at the BCO density. It is an important quantity for the interpretation of ice core records, where both, the isotopes in the ice, as well as the enclosed gases act as a proxy for the past climate. However, the chronologies of the ice and the gas phase differ. Because of the high porosity, the air in the firn can diffuse vertically and gets consistently exchanged with the atmospheric air, before the pores become sealed off, so that the trapped air initially has an age of only 7 to 30 years. The age difference Δage between ice and gas is thus given by the BCO age minus the age of the air at the BCO density and is needed to align the chronologies of the two parts. It lies typically on time scales of hundreds to thousands of years (Schwander et al., 1997).

Firn air content

The firn air content is measured by the depth-integrated porosity (DIP). It can be obtained by integrating the porosity of the firn from the surface to the depth where the ice has attained the density of ice of $\rho_\mathrm{i} = 917\,\mathrm{kg\,m^{-3}}$, whereat the porosity is given by

$$s(z) = 1 - \frac{\rho(z)}{\rho_\mathrm{i}}, \tag{2.33}$$

with the firn density ρ.

2.3.4. Drivers of firn densification

Firn densification is in general assumed to be dependent on two variables: The accumulation rate and the temperature.

The accumulation rate determines how quick the load on a specific layer rises. Thus, the BCO age is low for high accumulation rates, because the load on a layer increases rapidly. The firn thickness on the other hand is increased, when the accumulation is high, because the firn is buried quicker.

The temperature is important because all of the above-mentioned densification mechanisms proceed faster at high temperatures. Warm temperatures accordingly correspond to a low age and depth of the firn at the firn-ice transition.

However, the firn properties cannot always be described accurately by only using these two parameters, as for example Simonsen et al. (2013) have observed. This gap can potentially be explained by the impact of horizontal strain rates, respectively stresses, which were suggested by Alley and Bentley (1988) to affect the firn densification in the shear margins of ice streams, where high horizontal strain rates are present.

3. Firn densification modelling

Firn densification models are in general developed in order to infer some property of the firn such as the BCO age, the BCO depth or the DIP at a specific location from the local climatic conditions (Lundin et al., 2017), whereat two main application areas can be identified.

The DIP is required for estimating the mass of an ice sheet from radar altimetry, where the DIP needs to be subtract from the ice thickness, before it can be converted into mass. Of particular interest in this context is the estimation of the ice sheet mass balance, which directly corresponds to the contribution of the ice sheet to sea level change. The mass balance cannot be derived directly from the change of the surface elevation, because the contribution from a variable firn thickness can be as big as the contribution from variations of the accumulation rate (e.g. Braithwaite et al., 1994; Helsen et al., 2008; Alexander et al., 2019).

The second important application field for firn densification models is the estimation of the age difference Δage between the ice and gas records in ice cores. For the correct interpretation of the ice core data, knowledge about the BCO age and its past variability is crucial, which can be inferred from densification models. Additionally, firn air processes are modelled in order to estimate the age of the air at the BCO depth (e.g. Schwander et al., 1997; Buizert et al., 2015).

Empirically tuned firn densification models that assume steady state like the Herron-Langway model (Herron and Langway, 1980) are widely used, because they prove to represent the firn conditions well for a wide range of climatic conditions. Nonetheless, the development of a physically-based firn densification model is highly desired. Attempts to

model directly specific physical processes that are involved in the densification of firn are being made (Alley, 1987; Arnaud et al., 2000; Fourteau et al., 2020), but so far no complete process-based model for the densification of firn exists. Progress is being made by the development of semi-empirical models that are adapted to certain physical process and that are tuned with directly measured densification rates (Arthern et al., 2010). Mentionable is also the approach of the Crocus model in which the densification rate is modelled according to the viscosity and the load (Brun et al., 1992; Vionnet et al., 2012).

In this thesis the Herron-Langway model is used as a basis for modelling the impact of horizontal strain rates on the firn compaction. The model is favourable, because it exists in a load-based formulation and thereby takes into account a strain rate induced change of the load. Moreover, it demonstrates its applicability for the climatic conditions that are present in the studied area by reproducing the density profile of a local firn core well.

3.1. The Herron-Langway model

The Herron-Langway model (Herron and Langway, 1980), which was empirically tuned with depth-density data from Greenlandic and Antarctic ice cores, is the most established densification model. Despite its empirical character it proved to describe the firn properties well at many locations, particularly in Greenland.

In the derivation the firn is assumed to be in steady state, as described by Sorge's law (Bader, 1954)

$$\rho = f(z), \tag{3.1}$$

which states that for a fixed location the firn density is a function of depth, but invariant with time, if the climatic conditions do not change. The temperature and accumulation rate are therefore assumed to be

constant.

From the assumption that during the densification the change of the porosity is proportional to the overburden load, as suggested by Robin (1958), Herron and Langway derived the densification rate to be of the form

$$\frac{\mathrm{D}\rho}{\mathrm{D}t} = k\,\dot{b}^{a}(\rho_{\mathrm{i}} - \rho), \tag{3.2}$$

with the accumulation rate $\dot{b}$ and the Arrhenius-type temperature equation

$$k = \kappa \exp\left(-\frac{Q}{RT}\right), \tag{3.3}$$

where $R = 8.314\,\mathrm{J\,mol^{-1}\,K}$ is the gas constant and T the temperature, given in Kelvin. The exponent of the accumulation rate a, the prefactor κ and the activation energy Q were empirically tuned for the first two firn stages according to the ice core data. The resulting densification rate equations for the two stages are given by

$$\begin{aligned} \frac{\mathrm{D}\rho}{\mathrm{D}t} &= 11 \exp\left(-\frac{10160}{RT}\right) \dot{b}\,(\rho_{\mathrm{i}} - \rho) && \text{for } \rho \leq \rho_{\mathrm{crit}}, \\ \frac{\mathrm{D}\rho}{\mathrm{D}t} &= 575 \exp\left(-\frac{21400}{RT}\right) \dot{b}^{0.5}\,(\rho_{\mathrm{i}} - \rho) && \text{for } \rho > \rho_{\mathrm{crit}}, \end{aligned} \tag{3.4}$$

where $\rho_{\mathrm{crit}} = 550\,\mathrm{kg\,m^{-3}}$ is the critical density. The activation energies are likely underestimated in the Herron-Langway model with values of $10.16\,\mathrm{kJ\,mol^{-1}}$ and $21.4\,\mathrm{kJ\,mol^{-1}}$ that are significantly lower than the measured values of $42\,\mathrm{kJ\,mol^{-1}}$ for grain-boundary sliding and $60\,\mathrm{kJ\,mol^{-1}}$ for power-law creep. Thus, the Herron-Langway model is less sensitive to variations of the temperature, compared to a semi-empirical densification model like the Arthern model (Arthern et al., 2010) which uses process-based activation energies.

Additional formulations

As the Herron-Langway model assumes steady-state, from this dynamic formulation of the Herron-Langway model, an analytic formulation of the

form of Eq. (3.1) can be derived.

Additionally, a load-based version was suggested by S. J. Johnsen, where the densification rate of the second firn stage in correct form becomes

$$\frac{\mathrm{D}\rho}{\mathrm{D}t} = \frac{575^2 \exp\left(-\frac{42800}{RT}\right)}{\rho_\mathrm{w} g} \frac{(\sigma - \sigma_\mathrm{crit})(\rho_\mathrm{i} - \rho)}{\ln\left[(\rho_\mathrm{i} - \rho_\mathrm{crit})/(\rho_\mathrm{i} - \rho)\right]}. \tag{3.5}$$

In this equation ρ_w is the density of water, g the gravitational acceleration, σ the load and σ_crit the load at the critical density (Lundin et al., 2017). Note that because the Arrhenius equation is squared during the derivation, the activation energy in the second firn stage has factually doubled and thereby agrees better with the activation energies of the identified firn densification mechanisms. In the following, the Herron-Langway model is used in this load-based formulation, so that a local reduction of the load by pure shear is considered.

3.2. The Community Firn Model

The model experiments in this thesis are conducted within the model framework of the Community Firn Model (CFM) developed by Stevens et al. (2020). In this section a summary of the key features of the CFM is given. For a detailed introduction the reader is referred to Stevens et al. (2018) and Stevens et al. (2020).

The CFM is an open-source framework that comprises several firn densification models, which among others are the models by Herron and Langway (1980), Arnaud et al. (2000) and Arthern et al. (2010). In addition it contains several modules that incorporate physical processes that are relevant for firn densification under certain conditions.

The individual firn densification models in the CFM are implemented in an dynamic form, so that the response of the different firn properties to changing climatic conditions can be modelled. The model domain is one-dimensional. It consist of a fixed number of firn layers with uniform

properties each, which means that horizontal inhomogeneities are not considered.

The vertical movement of the firn layers is implemented with an Lagrangian approach. At each time step, if there is accumulation, a new firn layer is added on top of the firn column, while the bottom layer is removed. The properties of the upper layer are set by the forcing parameters and subsequently the changes of the properties of the remaining layer, such as density, temperature, age and depth, are computed and applied, according to the selected firn densification model. Because the number of firn layers is fixed, the thickness of the firn column is variable.

A model run in general consists of two phases: First, a spin-up run with constant climatic conditions is executed until the model is in steady state. Second, the main run is conducted with variable forcing parameters. The spin-up and the main run both follow the Lagrangian procedure described above.

The settings for a model run are given in a configuration file in the `.json`-format. In this file, the densification model and the initial size of the model are for example specified and optional modules are activated. It also contains the file paths to the forcing data, which is given as `.csv`-files with two rows, where one is for the time and one for the forcing parameter values. The model output is given in a `.hdf5`-file. Its content can also be specified in the configuration file.

3.2.1. Core modules

Density

For each firn layer the densification rate $\mathrm{D}\rho/\mathrm{D}t$ is determined according to the selected densification model, as exemplarily given in Eqs. (3.4) and (3.5). Subsequently the density is adjusted by

$$\rho_{\mathrm{new}} = \rho_{\mathrm{old}} + \left(\frac{\mathrm{D}\rho}{\mathrm{D}t}\right) \mathrm{d}t, \tag{3.6}$$

where dt is the length of the time step.

Temperature

In firn, heat is in general transported by diffusion and advection. The Lagrangian approach of the CFM implicitly takes account of the latter, so that only the equation for one-dimensional heat diffusion needs to be solved:

$$\rho c \frac{\partial T}{\partial t} = \frac{\partial}{\partial z}\left(k_{\mathrm{T}} \frac{\partial T}{\partial z}\right) + S, \tag{3.7}$$

where c and k_{T} are the specific heat capacity and the thermal conductivity of the firn, which are implemented in the CFM following the parametrisations given in Cuffey and Paterson (2010) by Yen (1981) and Schwerdtfeger (1963). S is a source term, which in general is neglected and set to zero, but will be considered in this study, when assessing the effect of strain heating. In the CFM Eq. (3.7) is solved with a fully-implicit finite-volume scheme. By default the surface temperature of the time step is applied as a Dirichlet boundary condition at the surface and at the bottom a Neumann boundary condition is used, where the temperature gradient is set to zero (Stevens et al., 2020). As the firn thickness is small compared to the thickness of the GrIS, these assumptions are also justified in the scope of this study.

3.2.2. Optional modules

The CFM moreover includes several additional modules for physical processes, such as meltwater percolation or firn-air diffusion, that are only relevant at certain locations or for specific applications of firn densification modelling. The current version of the CFM moreover already contains a module for layer thinning by horizontal strain rates, which however only considers the effect of pure shear. The modules for strain softening and strain heating, which are developed in the following, are accordingly implemented as optional modules as described in Appendix A.3.

3.2.3. Applied settings

In this thesis, the CFM is used only with the core modules for the temperature and density evolution of the firn and the optional modules that model the influence of horizontal strain rates, namely the module for pure shear, that is already implemented, and the modules for strain softening and strain heating, which are developed in the following.

For determining the densification rate, the load-based formulation of the Herron-Langway model is always applied. The initial thickness is set to 100 m. The spin-up time is adjusted such that the whole initial firn column is replaced and for the main run 400 yr-long chronologies of the input parameters with a monthly resolution are created. During the spin-up run, the mean values of the forcing parameters of the main run are used and in the main run, the average accumulation rate over the lifetime is used for each layer.

3.3. Firn densification in the presence of horizontal strain rates

In this section the model for the impact of strain softening on the process of firn densification is developed.

3.3.1. The vertical strain rate in classical models

A classical densification model only considers a normal strain rate in vertical direction, so that the strain rate tensor for some depth z is given by

$$\dot{\boldsymbol{\varepsilon}}_{\mathrm{c}} = \begin{pmatrix} 0 & 0 & 0 \\ 0 & 0 & 0 \\ 0 & 0 & \dot{\varepsilon}_{zz,\mathrm{c}} \end{pmatrix}, \tag{3.8}$$

where the vertical strain rate of the classical model is denoted as $\dot{\varepsilon}_{zz,\mathrm{c}}$. The first invariant of this tensor is not zero ($\dot{\varepsilon}_{\mathrm{I}} = \dot{\varepsilon}_{zz,\mathrm{c}} \neq 0$). Hence,

the ice is not incompressible, as expected for a densification process. The vertical strain rate that a specific densification rate causes can be derived from mass conservation to be given by

$$\dot{\varepsilon}_{zz,\mathrm{c}} = -\frac{1}{\rho}\left(\frac{\mathrm{D}\rho}{\mathrm{D}t}\right)_{\mathrm{c}}, \tag{3.9}$$

see (Morris and Wingham, 2014). Thus, the vertical strain rate of the classical model is directly proportional to the corresponding densification rate. Note that the minus accounts for the fact that by definition the strain rate is negative for compression.

Similar to the assumption of proportionality between strain rate and stress that is made in the derivation of the generalised Glen's flow law (2.26), it can be assumed that the strain rate is proportional to the load σ and scales with the effective viscosity η_{c} of the firn:

$$\dot{\varepsilon}_{zz,\mathrm{c}} = -\frac{\mathrm{k}}{\eta_{\mathrm{c}}}\sigma, \tag{3.10}$$

where k is some characteristic proportionality constant that will not be affected by horizontal strains, see also Eq. (2.32). Note that without limitations this densification creep relation does not imply the assumption of isotropy and incompressibility that is inherent in the generalisation of Glen's flow law.

Inserting this relation into Eq. (3.9) shows that the densification rate is proportional to the density and the load over the effective viscosity:

$$\left(\frac{\mathrm{D}\rho}{\mathrm{D}t}\right)_{\mathrm{c}} \propto \frac{\rho\sigma}{\eta_{\mathrm{c}}}. \tag{3.11}$$

3.3.2. The impact of horizontal strain rates

When not only the load, but also horizontal stresses affect the firn, horizontal strain rates are induced and the strain rate tensor, see Eq. (3.8), that describes the state of strain rates at a given depth adopts the more

complicated form of

$$\dot{\boldsymbol{\varepsilon}} = \begin{pmatrix} \dot{\varepsilon}_{xx} & \dot{\varepsilon}_{xy} & 0 \\ \dot{\varepsilon}_{xy} & \dot{\varepsilon}_{yy} & 0 \\ 0 & 0 & \dot{\varepsilon}_{zz} \end{pmatrix}. \tag{3.12}$$

In this case, the vertical strain rate $\dot{\varepsilon}_{zz}$ can potentially distinguish from the strain rate that a classical densification model would predict for the same climactic conditions ($\dot{\varepsilon}_{zz} \neq \dot{\varepsilon}_{zz,\mathrm{c}}$). A key step of this thesis is to find an expression for $\dot{\varepsilon}_{zz}$.

Therefore, the potential impact of the horizontal strain rates on the densification rate needs to be studied in detail. The firn compaction can be affected in two ways: By pure shear and by strain softening.

3.3.3. Pure shear

The term pure shear refers to the direct extension or compression of the firn column by horizontal strain. When the horizontal normal strain rates do not balance each other, i.e. $\dot{\varepsilon}_{\mathrm{I,H}} \neq 0$ in Eq. (2.17), mass balance requires a non-zero vertical strain rate. In first approximation this effect can be described by assuming incompressibility in Eq. (2.14), which gives

$$\dot{\varepsilon}_{zz,\mathrm{d}} = -\dot{\varepsilon}_{\mathrm{I,H}}, \tag{3.13}$$

where $\dot{\varepsilon}_{zz,\mathrm{d}}$ then is the vertical strain rate caused by pure shear. The complete vertical strain rate is then given by $\dot{\varepsilon}_{zz} = \dot{\varepsilon}_{zz,\mathrm{c}} + \dot{\varepsilon}_{zz,\mathrm{d}}$.

In a dynamical firn densification model this effect can be included by stretching or compressing each firn layer according to $\dot{\varepsilon}_{zz,\mathrm{d}}$ after each time step. Eventually the whole firn column as well as its vertical density profile will be stretched or compressed.

Apart from this direct stretching of the firn, the densification rate is affected by a change of the load. When for example the firn column gets compressed from the sides, it will get extended in vertical direction, whereby the load on each layer and hence the densification rate will

be increased. To consider this secondary effect, pure shear needs to be modelled within a load-based densification model, such as S. J. Johnsen's formulation of the Harron-Langway model (3.5). A module that incorporates the effect of layer thinning by pure shear is already implemented in the Community Firn Model (Stevens et al., 2020).

3.3.4. Strain softening

This effect was first suggested by Alley and Bentley (1988) to affect the firn densification in high-strain shear margins, but was not modelled before. The term strain softening describes the increased densification rate of the firn due to its Non-Newtonian behaviour, when being exposed to external stresses. It can be understood as a pseudoplastic behaviour, which means that the additional horizontal strain rates lead to a decrease of the effective viscosity of the firn, as it follows from Nye's generalisation of Glen's flow law by Eq. (2.30):

$$\eta = \left[2A^{1/n}\dot{\varepsilon}_{\mathrm{E}}^{m}\right]^{-1}, \tag{3.14}$$

where the creep parameter A and the creep exponent n are characteristic for the material and $m = 1 - 1/n$, so that $m = 2/3$ for $n = 3$.

The decreased viscosity then affects the densification rate according to Eq. (3.11), because

$$\left(\frac{\mathrm{D}\rho}{\mathrm{D}t}\right)_{\mathrm{c}} \propto \frac{1}{\eta_{\mathrm{c}}}. \tag{3.15}$$

When the densification rate of a classical firn densification model is known, it can be corrected for the effect of strain softening by multiplying it with a correction factor that is given by the ratio between the viscosity of the classical model and the reduced viscosity η_{c}/η, so that

$$\frac{\mathrm{D}\rho}{\mathrm{D}t} = \frac{\eta_{\mathrm{c}}}{\eta}\left(\frac{\mathrm{D}\rho}{\mathrm{D}t}\right)_{\mathrm{c}} \propto \frac{1}{\eta}. \tag{3.16}$$

Finding the correction factor

To determine the correction factor it is only necessary to know how the horizontal strain rates directly affect the viscosity. Other influencing factors, such as the density or the temperature, neglecting the effect of strain heating for the moment, do not differ between the original and the corrected model at the beginning of a specific time step. Therefore, the creep parameter A in Eq. (3.14) is the same for both models, so that the ratio between the viscosities of the classical and the corrected model is given by

$$\frac{\eta_\mathrm{c}}{\eta} = \frac{2A^{1/n}\dot{\varepsilon}_\mathrm{E}^m}{2A^{1/n}\dot{\varepsilon}_\mathrm{E,c}^m} = \left(\frac{\dot{\varepsilon}_\mathrm{E}}{\dot{\varepsilon}_\mathrm{E,c}}\right)^m . \tag{3.17}$$

The correction factor therefore only depends on the effective strain rate of the classical model, given by

$$\dot{\varepsilon}_\mathrm{E,c} = \left[\frac{\dot{\varepsilon}_{zz,\mathrm{c}}^2}{2}\right]^{1/2} \tag{3.18}$$

and on the corrected effective strain rate that also contains the horizontal strain rate components:

$$\begin{aligned} \dot{\varepsilon}_\mathrm{E} &= \left[\frac{1}{2}\left(\dot{\varepsilon}_{xx}^2 + \dot{\varepsilon}_{yy}^2 + \dot{\varepsilon}_{zz}^2\right) + \dot{\varepsilon}_{xy}^2\right]^{1/2} \\ &= \left[\frac{\dot{\varepsilon}_1^2 + \dot{\varepsilon}_2^2 + \dot{\varepsilon}_{zz}^2}{2}\right]^{1/2} . \end{aligned} \tag{3.19}$$

In the second step, the principle horizontal strain rates are inserted, following Eq. (2.20).

Equation (3.19) shows however that the corrected effective strain rate does not only depend on the horizontal stain rates, which are known, but also on the corrected vertical strain rate $\dot{\varepsilon}_{zz}$, which is the sought quantity. This problem can be circumvented by exploiting that the vertical strain rate of the densification is inversely proportional to the viscosity, as given

in Eq. (3.10). It follows that

$$\frac{\dot{\varepsilon}_{zz}}{\dot{\varepsilon}_{zz,\mathrm{c}}} = \frac{\frac{\mathrm{k}\sigma}{\eta}}{\frac{\mathrm{k}\sigma}{\eta_\mathrm{c}}} = \frac{\eta_\mathrm{c}}{\eta}, \tag{3.20}$$

where in the second step it is assumed that the load, which induces the densification of the firn, does not differ between the models. This assumption is justified, because any change of the load is already taken into account by the separate correction for pure shear. The constant of proportionality k will also not be affected by the horizontal strain rates.

Combining Eqs. (3.17) to (3.20) gives

$$\frac{\eta_\mathrm{c}}{\eta} = \frac{\dot{\varepsilon}_{zz}}{\dot{\varepsilon}_{zz,\mathrm{c}}} = \left(\frac{\dot{\varepsilon}_1^2 + \dot{\varepsilon}_2^2 + \dot{\varepsilon}_{zz}^2}{\dot{\varepsilon}_{zz,\mathrm{c}}^2} \right)^{m/2}. \tag{3.21}$$

To simplify this expression, two quantities can be defined: The first is the ratio between the corrected and the original vertical strain rate

$$r_\mathrm{V} \coloneqq \frac{\dot{\varepsilon}_{zz}}{\dot{\varepsilon}_{zz,\mathrm{c}}} \left(= \frac{\eta_\mathrm{c}}{\eta} \right), \tag{3.22}$$

which is also equal to the correction factor for the viscosities.

The second quantity is defined as the ratio between the effective horizontal strain rate and the effective strain rate of the classical model, given by

$$r_\mathrm{H} \coloneqq \left(\frac{\dot{\varepsilon}_1^2 + \dot{\varepsilon}_2^2}{\dot{\varepsilon}_{zz,\mathrm{c}}^2} \right)^{1/2}. \tag{3.23}$$

Note that every component of this second quantity is known, either from velocity maps or from the classical densification model.

Using these quantities, Eq. (3.21) can be rewritten as

$$r_\mathrm{V} = \left(r_\mathrm{H}^2 + r_\mathrm{V}^2 \right)^{m/2}. \tag{3.24}$$

Asumming a non-Newtonian flow behaviour of the firn with $n = 3$, the

exponent $m = 2/3$ can be inserted, which gives

$$r_{\mathrm{V}}^3 - r_{\mathrm{V}}^2 = r_{\mathrm{H}}^2. \tag{3.25}$$

This cubic relation contains the two quantities r_{H}, which is known, and r_{V}, which is the correction factor for the densification rate that is sought. Thus, Eq. (3.25) needs to be solved for r_{V}. Because the solution path would exceed the scope of this thesis, the solution is just presented, which is given by

$$r_{\mathrm{V}} = \frac{1}{3}\left(\kappa + \frac{1}{\kappa} + 1\right), \tag{3.26}$$

with

$$\kappa = \left[\frac{27}{2} r_{\mathrm{H}}^2 + \frac{3}{2}\left(81 r_{\mathrm{H}}^4 + 12 r_{\mathrm{H}}^2\right)^{1/2} + 1\right]^{1/3}. \tag{3.27}$$

The quantity r_{V}, which is equal to the correction factor $\frac{\eta_{\mathrm{c}}}{\eta}$ can now be used to correct the densification rate of a classical firn densification model for the effect of pseudoplastic densification, as given by Eq. (3.16).

3.3.5. Regularisation

Because the correction factor, according to Eq. (3.25), only depends on the ratio of the effective horizontal strain rate to the effective strain rate of the classical model Eq. (3.23), the correction factor has a singularity at the density of ice of $917\,\mathrm{kg\,m^{-3}}$, where the ice cannot densify further and the vertical strain rate $\dot{\varepsilon}_{zz,\mathrm{c}}$ becomes zero. This causes the model for strain softening to approach the density of ice in unrealistic short time and eventually evokes a numerical error.

To circumvent this problem, a regularisation is introduced. Inspired by *regularised Glen's flow law* (Greve and Blatter, 2009, Ch. 4) a *residual strain rate* $\dot{\varepsilon}_0$ is added to the vertical strain rate to ensure a finite correction factor:

$$r_{\mathrm{H}} \coloneqq \left(\frac{\dot{\varepsilon}_1^2 + \dot{\varepsilon}_2^2}{\left(\dot{\varepsilon}_{zz,\mathrm{c}} + \dot{\varepsilon}_0\right)^2}\right)^{1/2}. \tag{3.28}$$

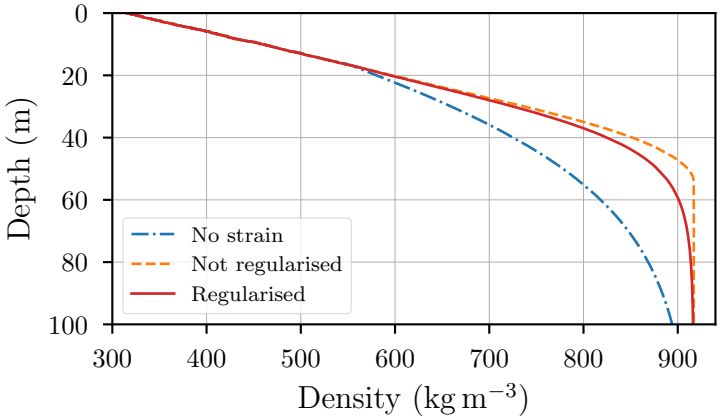

Figure 3.1.: Depth-density profile for shear margin conditions modelled with the classical Herron-Langway model and the extension for strain softening with and without applying a regularisation of $\dot{\varepsilon}_0 = -2 \times 10^{-4}\,\mathrm{yr}^{-1}$.

Leaving the perspective of firn densification modelling, the residual strain rate can be associated with the general thinning of firn and ice layers in ice sheets that is induced by the flow of ice towards the margins of the ice sheet. The corresponding vertical strain rate is approximately $-2 \times 10^{-4}\,\mathrm{yr}^{-1}$, which is set as the residual strain rate. A description of this approximation is given in Appendix A.1.

Figure 3.1 shows an example of a firn density profile that was modelled without the regularisation in comparison to one profile where the regularisation is applied as described above and one without the effect of strain being considered. Because of the numerical instability of the model without the regularisation, the profile for no regularisation was in fact created with a very small residual strain rate of only $-1 \times 10^{-40}\,\mathrm{yr}^{-1}$. Nonetheless, it clearly shows an unphysical behaviour at the density of ice, where a sharp transition from a high densification rate to no further densification can be seen. With the regularisation the transition is much smoother and therefore physically more realistic. The regularised profile resembles the density profile of a classical model without strain,

while not changing the rate of firn thinning by pseudoplastic densification considerably.

3.3.6. Strain heating

Strain heating refers to the internal heating of the firn by dissipation due to its deformation. It is given as the product of the stress tensor with the strain rate tensor. Thus, the source term in Eq. (3.7) reads as

$$S_{\mathrm{sh}} = \sigma_{ij}\dot{\varepsilon}_{ij} = \mathrm{tr}(\boldsymbol{\sigma}\dot{\boldsymbol{\varepsilon}}), \tag{3.29}$$

where the Einstein notation is used in the first step (Holschuh et al., 2019).

Because the stress is not known, the source term can be reformulated, following Greve and Blatter (2009, Ch. 5), by employing the definition of the stress deviator (2.7), the viscosity (2.29), the load (2.6) and the effective strain rate (2.15) as follows:

$$\begin{aligned} S_{\mathrm{sh}} &= \mathrm{tr}(\boldsymbol{\sigma}\dot{\boldsymbol{\varepsilon}}) \\ &= \mathrm{tr}([\boldsymbol{\tau} - p\mathbf{I}]\dot{\boldsymbol{\varepsilon}}) \\ &= \mathrm{tr}(\boldsymbol{\tau}\dot{\boldsymbol{\varepsilon}}) - p\,\mathrm{tr}(\dot{\boldsymbol{\varepsilon}}) \\ &= 2\eta\,\mathrm{tr}\left(\dot{\boldsymbol{\varepsilon}}^2\right) - \sigma\,\mathrm{tr}(\dot{\boldsymbol{\varepsilon}}) \\ &= 4\eta\dot{\varepsilon}_{\mathrm{E}}^2 - \sigma\,\mathrm{tr}(\dot{\boldsymbol{\varepsilon}}). \end{aligned} \tag{3.30}$$

As the viscosity η and the load σ are already computed in the CFM, strain heating can easily be implemented with this expression.

4. Data

This chapter details the external data that is used in this study. The first part presents the input data that is used for the forcing of the densification model and describes how it is processed. In the second part, several firn surveys which were conducted in area of NEGIS around EGRIP are described, which are used to assess the accuracy and applicability of the developed model.

4.1. Model forcing

4.1.1. Ice velocity

Horizontal strain rates are deduced from the ice velocity according to Eq. (2.13). For this purpose the MEaSUREs Multi-year Greenland Ice Sheet Velocity Mosaic (Joughin et al., 2016) by Joughin et al. (2018) is applied, which covers the whole GrIS with a spatial resolution of $250\,\mathrm{m} \times 250\,\mathrm{m}$. The dataset shows artefacts in the velocity with diagonal orientation with respect to the data grid. They are removed by applying a Gaussian filter with a smoothing length of $\sigma = 3$ in order to avoid a clear overestimation of the horizontal strain rates along the artefacts. In this process the effective spatial resolution is however lowered and features in the velocity field on the order of a few hundred meters are smoothed out.

From the smoothed velocity map the normal and shear strain rates in x- and y-direction are determined first and then used to compute the principle horizontal strain rates. The strain rate chronology for a specific

location is then obtained by stepwise calculating the previous flow path back in time according to the velocity and interpolating the horizontal strain rate onto the current position at each time step.

The velocity field and the derived strain rate components are shown exemplarily for the region of NEGIS in Fig. 4.1. In the upper part, where EGRIP is located, the ice stream has a flow velocity of around $50\,\mathrm{m\,yr^{-1}}$ and even higher velocities downstream (Figure 4.1a). Along the margins of NEGIS, where the ice enters the ice stream, high strain rates can be observed. The normal and shear strain rates have opposing signs between the two shear margins (Figures 4.1b to 4.1d). So that it is more convenient to work with the principle strain rates (Figures 4.1e and 4.1f), where the first one is always positive and compressive and the second negative and tensile. Merely at few locations in the outer part of the ice stream, where the ice is compressed strongly, both components are positive.

The vertical strain rate in Fig. 4.1g represents the effect of pure shear, which corresponds to the imbalance between the compressive a tensile strain rates (note the lower value range). Within the ice stream and the shear margins it is generally higher than outside, but it does not follow a distinct pattern. It diverges locally between spots, where the ice column is compressed and spots, where it is stretched. Figure 4.1g moreover shows small vertical strain rates outside the ice stream, which tells that the assumption of no horizontal strain in general does not hold for firn densification.

The lower firn thickness in the shear margins and the existence of the shear margin troughs cannot be explained by pure shear, because the vertical strain rate has no structure that would allow such an argument. Hence, the effective horizontal strain rate (Figure 4.1h) is likely the decisive quantity. In the shear margins consistently high values of generally more than $3\times10^{-3}\,\mathrm{yr^{-1}}$ can be observed, compared to effective horizontal strain rates of much less than $1\times10^{-3}\,\mathrm{yr^{-1}}$ in the interior and outside of the ice stream.

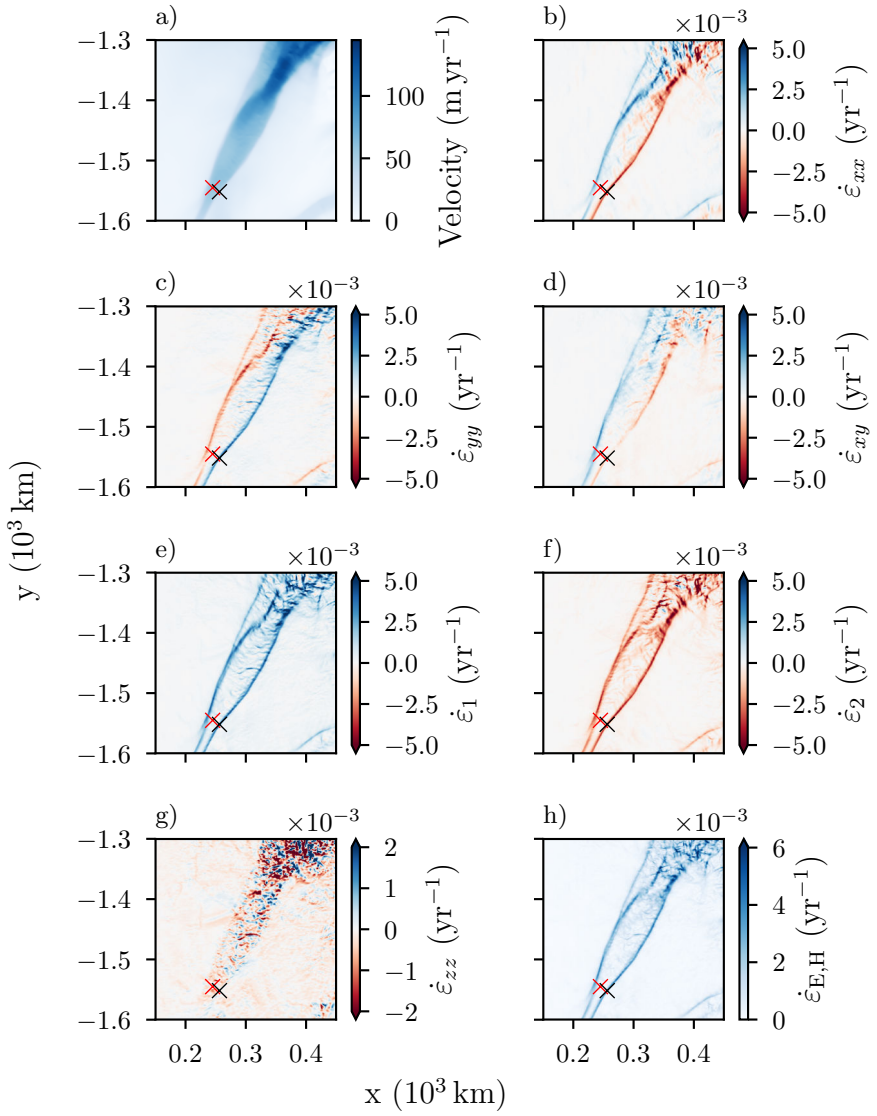

Figure 4.1.: Maps of the central part of NEGIS of (a) the total ice flow velocity from Joughin et al. (2016), (b–c) the normal horizontal strain rates in x- and y-direction, (d) the horizontal shear strain rate, (e–f) the principle horizontal strain rates, (g) the vertical strain rate from pure shear and (h) the effective horizontal strain rate.

4.1.2. Regional climate model HIRHAM5

The firn densification model is forced at the surface with the output data of the latest version of the RCM HIRHAM5 (Langen et al., 2017; Mottram et al., 2017). On the lateral boundaries HIRHAM5 is forced by the ERA-Interim reanalysis product (Dee et al., 2011) It runs on a $0.05° \times 0.05°$ rotated polar grid, which corresponds to a resolution of $\sim$5 km. The RCM covers the period of 1980 to 2014. The model output is provided as daily, monthly and annual means. Additionally, HIRHAM5 was forced with NorESM (Bentsen et al., 2013) to run the model for 20 years with pre-industrial conditions (R. Mottram, unpublished, personal communication, 2020).

From the monthly means of the HIRHAM5 output, 400 year-long climate chronologies are created, which are used to force the firn densification model at the surface. Before 1980 the 20 yr-output for pre-industrial conditions is used repeatedly to extend the chronology back in time. Simultaneous to the creation of the strain rate time series, the chronologies for the temperature and accumulation rate are obtained by interpolating the current climate fields onto the current position at each time step. In this way temporal as well as spatial variability is taken into account.

For the location of EGRIP, the accumulation rate over the time span averages $0.11\,\mathrm{m.\,i.e.\,yr^{-1}}$ which agrees well with the mean accumulation rate found by Vallelonga et al. (2014). The mean temperature at EGRIP from the HIRHAM5 output in the last 3 years of the history amounts to $-26.9\,°\mathrm{C}$, which is $2.1\,°\mathrm{C}$ warmer than the mean surface temperature of $-29.0\,°\mathrm{C}$ that was recorded at the EGRIP-PROMICE automatic weather station between 2016 and 2019 (Fausto and Van As, 2019). Although the two time intervals do not overlap, the difference is interpreted as a bias in the HIRHAM5 temperature, because such an abrupt shift of the mean temperature is improbable and also because the temperature in Greenland tends to be rising and not sinking. Hence, the temperature chronologies for the NEGIS region are corrected for this bias.

Moreover, the multi-year average of the HIRHAM5 output is employed to model the firn air content of the entire Greenland ice sheet. Therefore, the HIRHAM5 output is interpolated linearly onto the grid of the ice velocity maps. As Mottram et al. (2017) state, the RCM likely underestimates melt and precipitation rates and, as seen for EGRIP, the temperature might be overestimated in the model. Despite these issues, the output fields allow to estimate the spatial variability of the climatic conditions on the ice sheet and in general reproduce the climate in Greenland sufficiently well, to study characteristic properties of the ice sheet.

4.1.3. Surface density

A surface density of $315\,\mathrm{kg\,m^{-3}}$ is assumed in all model runs, following Fausto et al. (2018). In the region around EGRIP this matches well with observed snow densities at the surface (Schaller et al., 2016). Elsewhere on the Greenland Ice Sheet this assumption may be less accurate, but for the model experiments conducted in this thesis, the potential bias can be neglected, because the main interest lies in the identification of relative differences between models and thereby approximately cancels out.

4.2. NEGIS firn surveys

In the interior of the Greenland ice sheet, high horizontal strain rates can be observed particularly in the shear margins of the North-East Greenland Ice Stream. In this region several surveys were undertaken in the recent years, in which the firn in the shear margins was examined with different approaches, see Fig. 4.2. This part presents the surveys that are employed in this thesis.

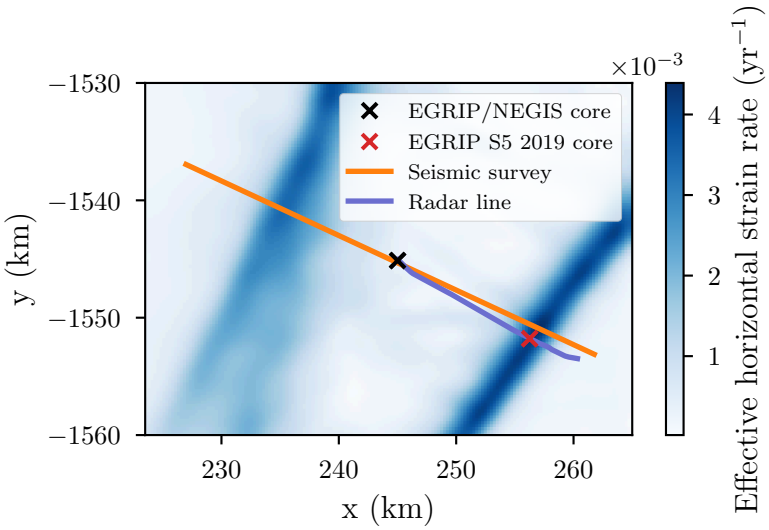

Figure 4.2.: Location of the firn surveys that were conducted at NEGIS in the proximity of EGRIP. In the background the effective horizontal strain rate is shown.

4.2.1. Firn cores

Besides the deep EGRIP ice core that is being drilled in the centre of the ice stream, several firn cores were drilled in the NEGIS region. Of particular interest for this study are the 67 m NEGIS firn core, which was drilled in the centre of the ice stream close to the site of the deep ice core (Vallelonga et al., 2014) and the EGRIP S5 2019 firn core (I. Koldtoft, unpublished, personal communication, 2019), drilled in the south-east shear margin of NEGIS. The latter was intended to be used to validate and adapt the model, but unfortunately could not be processed before the submission of this thesis, because of the cancellation of the 2020 field season due to the COVID-19 pandemic. Nonetheless, the firn core is modelled in this thesis as an example for the shear margin conditions, because of favourable features at the location of its drill site and an intersection with the radargram, presented in the following.

4.2.2. Radar survey

In 2019 a radargram was record from EGRIP across the south-east shear margin with a RAMAC 500 MHz GPR (D. A. Lilien, unpublished, personal communication, 2020), passing the location of the EGRIP S5 2019 firn core. It is employed in this thesis to estimate the variability of the accumulation rates in the NEGIS region, particularly in the shear margin troughs, and to assess the importance of horizontal strain rates for the interpretation of radar data.

To extract the mean accumulation rates along the radar line, a shallow layer is traced in the preprocessed radargram. The age of the layer is calibrated by locating its position in the NEGIS firn core, as follows. The theoretic two-way travel time of the NEGIS firn core is computed as detailed in Appendix A.2 and then the age of the traced layer is identified as the age of the firn at the point, where the two-way travel time of the firn core matches the two-way travel time of the closest data point in the traced layer. In this way, an age of 44 years could be ascertained, which corresponds to firn densities of only around $500\,\mathrm{kg\,m^{-3}}$, so that the layer lies in the first stage of firn densification and is not affected by horizontal strain rates.

This allows to determine the accumulation rates by employing the analytic Herron-Langway model. For a temperature of $-29\,^{\circ}\mathrm{C}$ and a range of potential accumulation rates, the analytic depth-density and -age profiles are modelled and the theoretic two-way travel time for the 44 yr-layer is computed. For each data point of the radar line, the accumulation is now assumed to be given by the accumulation rate of the model, for which the modelled two-way travel time of the 44 yr-layer is equal to the measured two-way travel time of the traced layer at the respective location.

In Fig. 4.3 the obtained accumulation rates are plotted against the surface elevation to get an estimate of the increased accumulation rate in the shear margins. The elevation was recorded along with the radargram, but possesses strong measurement artefacts, which are removed with a

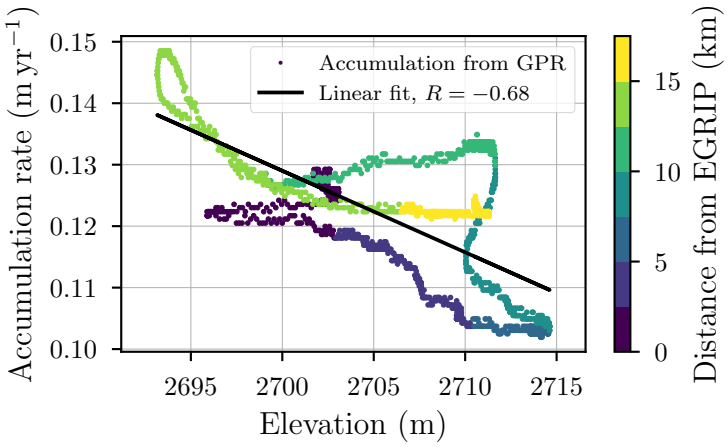

Figure 4.3.: Accumulation rate and corrected elevation of the ice sheet surface along the radar line from EGRIP across the South-East shear margin. In first-order approximation, the accumulation rates are proportional to the elevation with a correlation coefficient of $R = -0.68$.

Gaussian filter with a smoothing length of $\sigma = 20$. Additionally, it is corrected for a bias of 39.3 m compared to the elevation that was recorded along with the seismic reflection profile discussed below.

The distribution shows the tendency of high accumulation rates to occur at low elevations, which can be explained by the deposition of snowdrift in the shear margin troughs, where the accumulation rates are approximately 10 to 20 % higher than in the centre of the ice stream. The accumulation rate however is not only controlled by the elevation. Particularly at the edge of the shear margin around 10 km from EGRIP high accumulation rates are also observed at high elevations. The linear regression of the data gives a moderate correlation coefficient of $R = -0.68$. The elevation can hence be used in the first approximation as a proxy for the accumulation rate in the region of the NEGIS.

4.2.3. Firn density from seismic reflection profiles

In 2012 Riverman et al. (2019) have conducted a geophysical survey, where an almost 40 km-long seismic reflection profile was recorded along a cross-section of NEGIS that includes both shear margins, see Fig. 4.2. . The seismic waves were created by shooting Pentolite explosives with a spacing of 480 m between the shot locations. The seismic velocities were inferred from the travel time, that was recorded at 48 geophones, which were evenly spaced between −460 m and 480 m from the shot location. From the seismic velocities of the firn the densities were derived by calibrating the data with the seismic velocity at the drill site of the NEGIS firn core. Riverman et al. found the firn thickness to be reduced by up to 30 m in the shear margins and concluded that the thinner firn originates from the effect of strain softening on firn densification. The shot locations were obtained from Riverman (2018), in order to reproduce the firn density profile with the developed model for assessing the model accuracy.

5. Results

5.1. Sensitivity

As a first step, the sensitivity of firn densification to horizontal strain rates is examined with the developed model for climatic conditions that are characteristic for the dry-snow zone of the GrIS. Therefore, the model is run with uniform forcing, for various combinations of the temperature, accumulation rate and effective horizontal strain rate. The temperature is increased linearly between -29 and $-17\,°\mathrm{C}$ in steps of $2\,°\mathrm{C}$, the accumulation rate is varied logarithmically from 0.075 to $1\,\mathrm{m.\,i.e.\,yr^{-1}}$ and the effective horizontal strain rate is increased from 0 to $7 \times 10^{-3}\,\mathrm{yr^{-1}}$ in steps of $1 \times 10^{-3}\,\mathrm{yr^{-1}}$.

For each model run the density and age profiles, the BCO depth, BCO age and the DIP are computed. To ensure accuracy of the latter, the thickness of the model domain is adjusted for each run such that a porosity of less than $1\,\%$ is attained at the bottom.

5.1.1. Dependency on climatic conditions

Figure 5.1 shows how the DIP and BCO age depend on the climatic forcing according to the classical Herron-Langway model, which does not consider horizontal strain. Additionally, the figure shows the deviation of the respective quantities, when an effective horizontal strain rate of $3 \times 10^{-3}\,\mathrm{yr^{-1}}$ is applied.

Both quantities change the most at the climate where their value in case of no strain is also the highest. For an effective horizontal strain rate

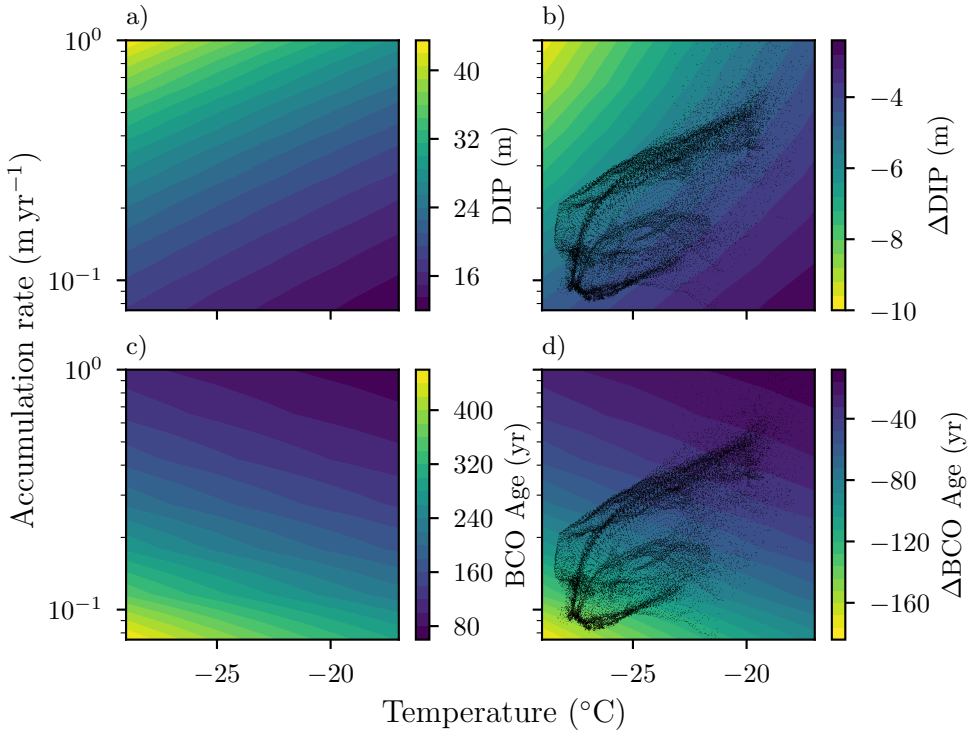

Figure 5.1.: Dependency of the DIP and BCO age on the climatic conditions. (a) The DIP in case of no strain, (b) its change, when an effective horizontal strain rate of $3 \times 10^{-3}\,\mathrm{yr}^{-1}$ is applied and (c) the BCO age and (d) its change for the same strain rates. On top of (b) and (d) the distribution of the combinations of temperature and accumulation rate are plotted, that according to the HIRHAM5 output occur in the dry-snow zone of the GrIS.

of $3 \times 10^{-3}\,\mathrm{yr}^{-1}$, which is a realistic value for the shear margins of an ice stream, the DIP decreases by 20 to 25 % and the BCO age is lowered by almost 40 % at very low accumulation rates and temperatures, but changes less strongly for higher values.

The distribution of the observed combinations of temperature and accumulation rate shows a rough proportionality between the two parameters. Comparing the distribution to the change of the DIP, almost all points lie in a range of 4 to 6 m. Thus, the DIP is mainly sensitive to the effective horizontal strain rate, but not to the climate. The BCO depth is approximately proportional to the DIP with about three times larger values, so that it behaves like the DIP and is not shown here explicitly.

The BCO age on the other hand is not only sensitive to the horizontal strain, but also to the climatic forcing at the specific location, because the distribution covers the whole range of modelled changes. Especially at cold temperatures and high accumulation rates, the horizontal strain rates can affect the BCO age significantly.

5.1.2. Sensitivity to the effective horizontal strain rate

To assess the sensitivity of firn densification to horizontal strain rates according to the presented model, the depth-density profile for a temperature of −25 °C and an accumulation rate of $\sim$0.274 m. i.e. yr^{-1}, which according to the HIRHAM5 output conform approximately with the mean conditions of the dry-snow zone of the GrIS, is plotted in Fig. 5.2 for the different applied effective horizontal strain rates.

The plot shows that especially high densities arise at a lower depth, when horizontal strain is applied. According to the model, even the density of ice of $917\,\mathrm{kg\,m}^{-3}$ is attained in the first hundred meters of the firn column, when the the effective horizontal strain rate is greater than $2 \times 10^{-3}\,\mathrm{yr}^{-1}$. Below the critical density of $550\,\mathrm{kg\,m}^{-3}$ the profiles, as expected, do not differ, because the module for strain softening only becomes active in the second firn stage.

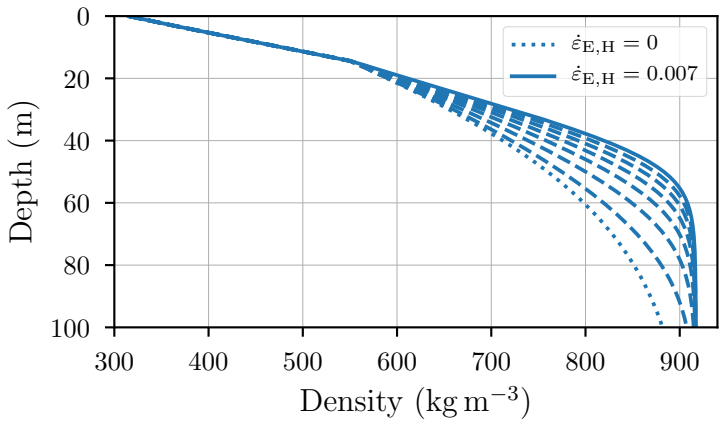

Figure 5.2.: Depth-density profile for the mean climatic conditions of the GrIS dry-snow zone for different effective horizontal strain rates. Starting from no strain (dotted line) the strain rate is increased gradually by $1 \times 10^{-3}\,\mathrm{yr}^{-1}$ (dashed lines) to a value of $7 \times 10^{-3}\,\mathrm{yr}^{-1}$ (solid line).

The plot moreover shows with increasing strain rate a decreasing distance between neighbouring lines, which means that according to the strain softening model, the sensitivity of the firn thickness to to the effective horizontal strain rate declines when the strain rates become high. The thinning of the firn at a strain rate of only $2 \times 10^{-3}\,\mathrm{yr}^{-1}$ is already half as big as the total thinning, when the effective horizontal strain rate amounts to $7 \times 10^{-3}\,\mathrm{yr}^{-1}$.

Firn age

In Fig. 5.3 the dependency of the age of the firn and ice on the effecfive horizontal strain rate is shown at different depth for the same forcing as used in Fig. 5.2. Additionally the contour lines of the critical density and the close-off density are shown. Similar to the density, a higher firn age is attained at shallower depth, when the firn is subjected to horizontal strain, whereat the sensitivity also decreases with an increasing strain rate.

This BCO age can be seen in the plot as the age of the firn at the

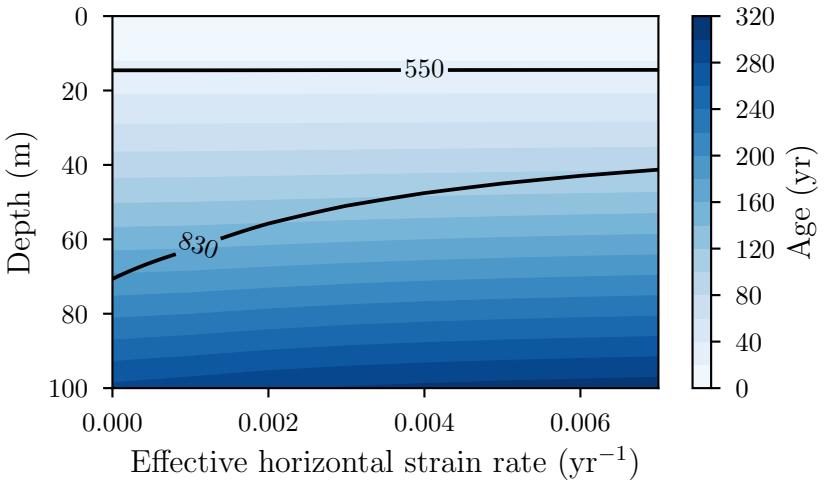

Figure 5.3.: Dependency of the depth-age relation of the firn on the effective horizontal strain rate. The contour lines indicate the depth of the critical density and the firn-ice transition at the BCO density.

close-off density. Because the density is generally affected stronger by the horizontal strain rates than the firn age, the BCO age behaves similar to the density. At a moderate effective horizontal strain rate of $2 \times 10^{-3}\,\mathrm{yr}^{-1}$ the firn age is already decreased by around 50 years from an age of $\sim$190 yr at no strain to an age of $\sim$140 yr. At an very high effective horizontal strain rate of $7 \times 10^{-3}\,\mathrm{yr}^{-1}$, however, the BCO age is only reduced by 40 more years.

In conclusion, the sensitivity of all firn properties to horizontal strains is high at low strain rates and declines for an increasing effective horizontal strain rate. Thus, the firn is generally affected strongly, when it is subjected to horizontal strain and already low strain rates can contribute considerably to the densification of the firn.

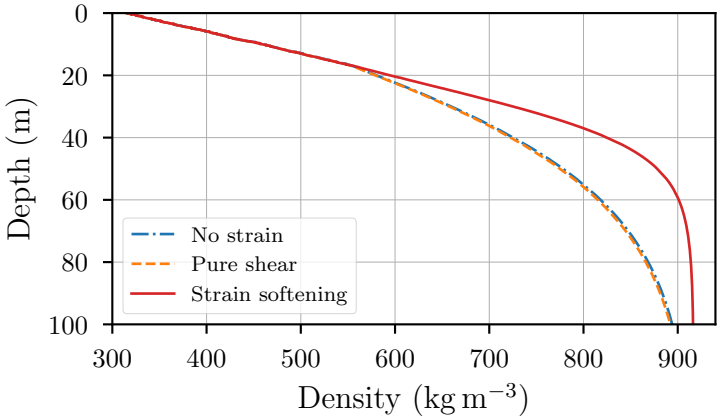

Figure 5.4.: Modelled firn density profiles for shear margin conditions when no strain, pure shear and strain softening are considered.

5.2. Densification mechanisms

To better understand the contribution of different densification mechanisms to the decreased firn thickness in the shear margins of ice streams, various possible mechanisms are modelled in the following for shear margin conditions.

5.2.1. Pure shear and strain softening

First, the effects of pure shear and strain softening of the firn are compared with each other. Figure 5.4 shows the density profiles of the EGRIP S5 2019 firn core, when it is modelled with the classical Herron-Langway model and with the module for pure shear and the one for strain softening being active.

When only pure shear is considered, the density profile does almost not differ from the profile created without strain. The firn thickness is only slightly extended, which means that the tensile horizontal strain rate at the drilling site of the firn core almost balances the compressive component. In contrast, strain softening gives rise to a significant reduction of the firn thickness. In comparison with the effect of pure shear,

strain softening is clearly the dominant strain-based firn densification mechanism.

5.2.2. Strain heating

As the densification of firn is sensitive to the temperature, horizontal strain rates can in principle also influence the densification rate indirectly via strain heating or can be accompanied by other variations of the temperature in the shear margins. Therefore, the shear margin firn core is modelled with the effect of strain heating as described in Section 3.2.1 and compared to the model for strain softening.

Additionally, the role of vertical upward heat transport that can occur in the shear margins is studied. This process was suggested by Holschuh et al. (2019) to be the dominant mechanism that controls the temperature in the shear margins. Holschuh et al. used data from an ice-penetrating radar to assess 3D-thermomechanical models of NEGIS and found the depth-averaged temperature in the South-East shear margin to be increased by 2 to 6 °C due to vertical heat transport. This effect can be modelled in good approximation by adding the respective deviation of the temperature on the forcing temperature, which leads to an increase of the temperature in the whole modelled firn column by exactly the same amount.

The results of these model runs are shown in Fig. 5.5. The effect of strain heating corresponds to the effect of an increased temperature by 1 to 2 °C, which all are not significant compared to the effect of strain softening. If the temperature in the firn were 6 °C higher, the thinning of the firn would be half as big as the thinning by strain softening. Because such a strong increase of the temperature is unlikely, vertical heat flow is probably also of minor importance for firn densification in the shear margins, its significance can however not be ruled out completely.

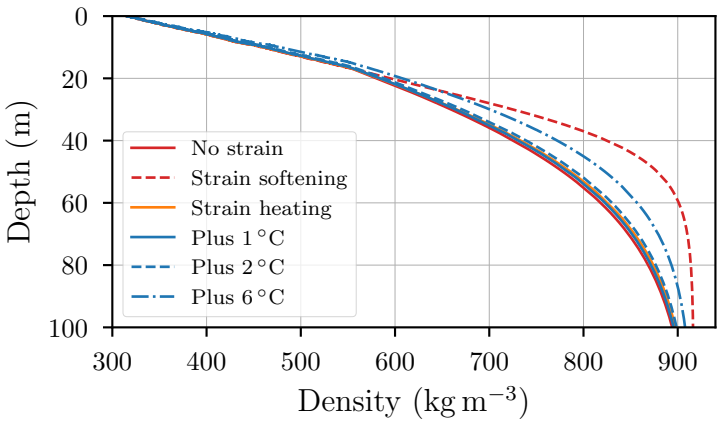

Figure 5.5.: Comparison of an enhanced firn densification by strain softening with the effects of strain heating and vertical upward heat transport.

5.3. NEGIS firn surveys

Various surveys in the shear margins of NEGIS were undertaken in the recent years. In this part, the firn at the survey sites, see Fig. 4.2, is modelled with the extension of strain-accelerated firn densification to test the applicability of the model and to assess the importance of strain softening for the interpretation of the data itself.

5.3.1. Firn cores

The NEGIS and EGRIP S5 2019 firn cores are modelled with and without the effect of strain being considered. The chronologies of the forcing parameters for their sites are compiled as described in Section 4.1. Because the mean accumulation rate of the HIRHAM5 output for the site of the shear margin firn core was lower and not by 10.9 % higher than at EGRIP, as derived from the radargram at the points of intersection of the firn cores, the accumulation rate chronology for the S5 firn core was scaled accordingly.

In Fig. 5.6 the depth-density profiles of the two firn cores are shown and compared to the data of the NEGIS firn core. The normal Herron-

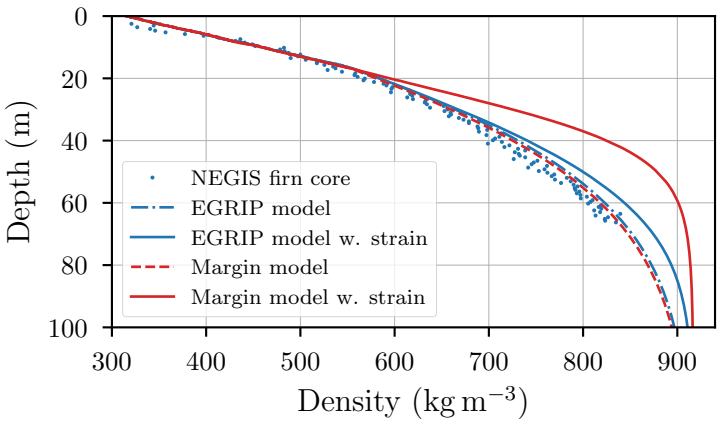

Figure 5.6.: Recorded and modelled depth-density profile of the NEGIS firn core and modelled EGRIP S5 2019 firn core. Both firn cores are modelled with the classical Herron-Langway model and with the extension for the impact of the horizontal strain rates by strain softening and pure shear.

Langway model agrees well with the data, whereas the firn thickness is underestimated by approximately 10 m, when the module for the effect of horizontal strain is activated. This suggests that the developed model is either too sensitive to low strain rates or the empirically tuned Herron-Langway model implicitly already considers a moderate effect of strain softening.

When strain is not considered, the modelled density profile of the shear margin firn core, is almost identical to the profile of the NEGIS firn core with merely a slightly higher firn thickness due to the higher accumulation rate. This suggests that significantly stronger variations of the accumulation rate than observed are needed, to affect the firn density in the shear margins considerably. On the contrary, when strain softening is included into the model, the modelled firn is substantially thinner in the shear margins than in the centre of the ice stream. This tells, that the effect of an increased accumulation rate in the shear margins is negligible compared to the deviation by strain softening.

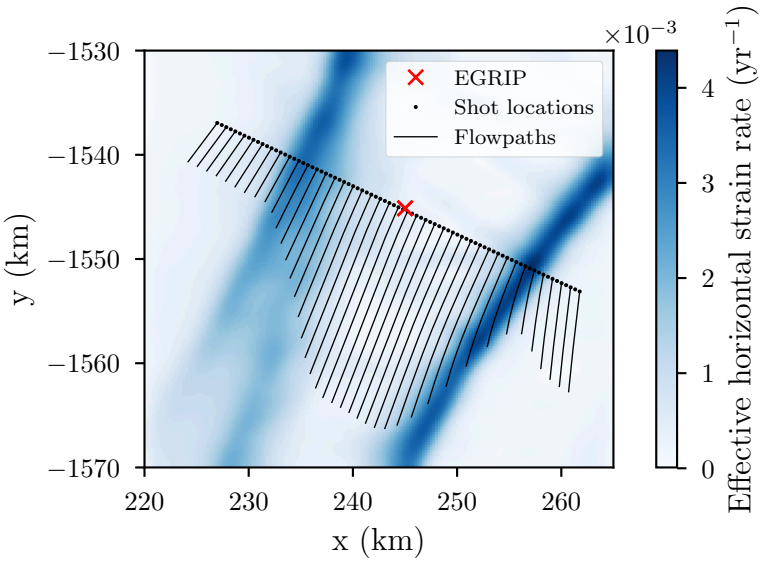

Figure 5.7.: Shot locations of the seismic survey conducted by Riverman et al. (2019) and flow paths over the firn age for every second shot location. In the background the effective horizontal strain rate is shown.

5.3.2. Firn density from seismic reflection profiles

Figure 5.7 shows the shot locations from the seismic reflection survey conducted by Riverman et al. (2019). According to the ice sheet velocity Mosaic from Joughin et al. (2016) the previous flow paths of the firn over the BCO age are reconstructed and shown for every second point. In the interior of the ice stream, where the ice flow velocities are the highest, the oldest firn at the seismic survey line originates around 20 km upstream and will have experienced significantly more climate variability than the oldest firn outside of the ice stream, which has only travelled for 5 to 10 km. The flow paths in the shear margins are particularly short due to the lower firn age and, as a consequence, lie almost entirely inside the shear margins. Hence, the corresponding firn has experienced high horizontal strain rates over almost the whole lifespan.

The horizontal strain rates along the flow paths of the past 400 yr are used to model the firn densities along the cross-section of NEGIS at the

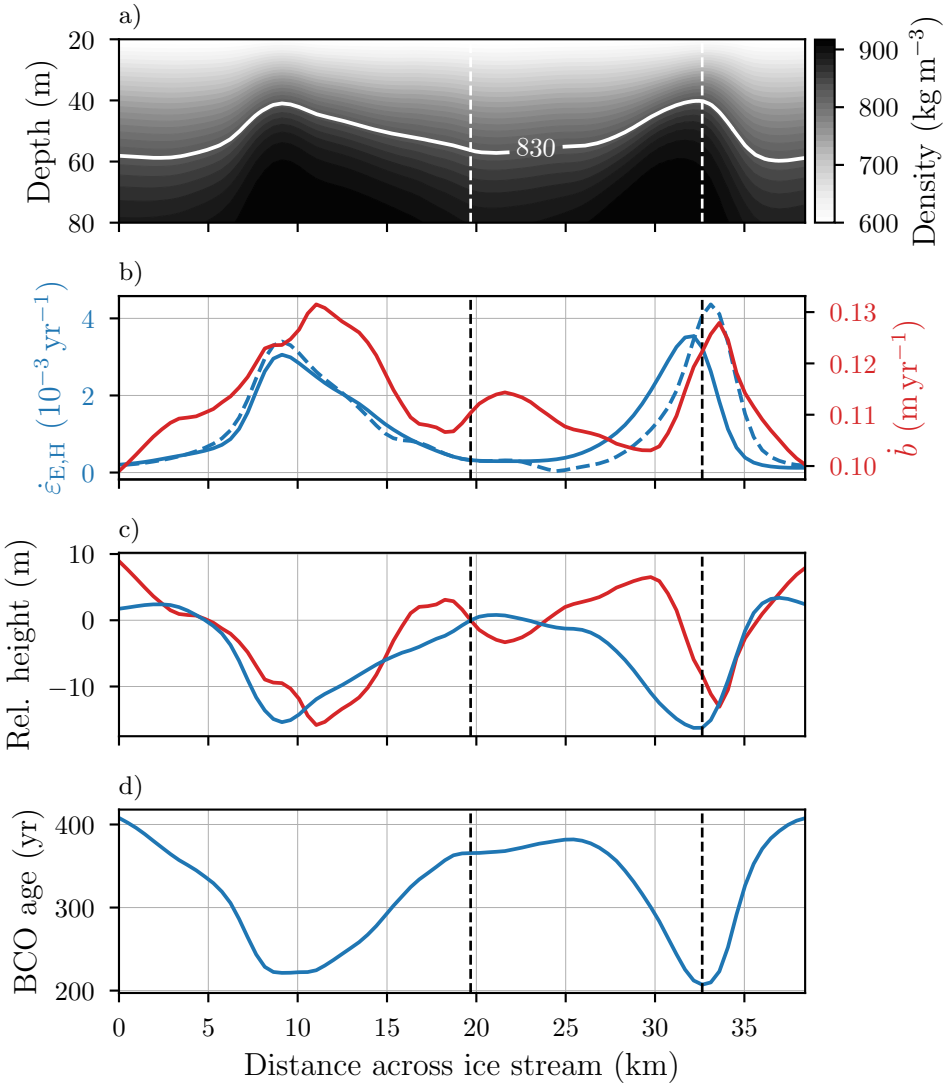

Figure 5.8.: (a) Modelled firn densities along the cross-section of NEGIS, where the seismic survey by Riverman et al. (2019) was conducted. The contour line of the BCO-density indicates the location of the firn-ice transition. (b) The mean effective horizontal strain rate and accumulation rate over the firn age (solid lines) and the effective horizontal strain rate at the location of the seismic survey (dashed blue line). (c) Deviation of surface elevation (red line) and firn thickness relative to EGRIP (blue line). (d) BCO age along the cross-section. The vertical dashed lines indicate the location of the NEGIS and EGRIP S5 2019 firn cores.

shot locations of the seismic survey. The temperature and accumulation rate histories for EGRIP, that were created as described in Section 4.1, are used to force the model, whereat the accumulation rate is scaled according to the elevation with the linear relation that was derived in Section 4.2.2. In this way, the effect of an increased accumulation rate in the shear margins is considered. Although, the accumulation rate does not perfectly correlate with the elevation, as seen in Fig. 4.3, this first-order approximation is sufficient for the scope of this study, because in any case the variations of the accumulation rate across NEGIS are not strong enough to affect the firn density substantially, as Fig. 5.6 shows. Using the temperature at EGRIP for the whole cross-section is also legitimated, because the monthly mean temperature does not vary considerably over the region.

The obtained firn density cross-section is displayed in Fig. 5.8a with a view in downstream direction. The profile shows a decreased firn thickness in the shear margins of approximately 20 m, which is indicated by the contour line of the close-off density of $830\,\mathrm{kg\,m^{-3}}$. The approximate location of the EGRIP S5 firn core is indicated by the right dashed line and lies in the region of the thinnest firn.

The density profile correlates very well with the mean effective horizontal strain rate over the firn age (solid blue line in Fig. 5.8b) and less with the mean accumulation rate (solid red line), which underlines that the effective horizontal strain rate is the dominant forcing parameter for the firn densification in the shear margins. The effective horizontal strain rate at the location of the seismic survey (dashed blue line) resembles the mean value, which indicates little variability of the horizontal strain rate over the firn age, which is in accordance with the short flow paths in the shear margins that were observed in Fig. 5.7. In first approximation the firn density in the shear margins can hence be modelled by the local strain rate conditions.

In Fig. 5.8c the deviation of the firn thickness (blue line) and the surface elevation (red line) relative to EGRIP are plotted. Both quantities

agree in the magnitude of their change, which suggests that the decreased surface elevation in the shear margins of an ice stream is caused by strain softening of the firn that is induced by the horizontal strain rates. However, the deepest points of the shear margin troughs are not perfectly aligned with the positions of the thinnest firn and the elevation profile possesses features like a valley near EGRIP, which are not reflected in the firn thickness. Other factors like the bedrock topography, the upstream surface elevation or the accumulation pattern must thus also affect the surface topography significantly.

Figure 5.8d lastly shows the BCO age along the cross-section, which is the age of the firn when the included gas bubbles become sealed off. According to the presented model it is around 50 % lower in the shear margins. For the correct interpretation of the isotope and gas records of ice cores that are drilled in the centre of an ice stream, it is therefore required to reconstruct the past flow path accordingly, because the time and location, where the ice has passed the shear margin, needs to be determined, in order to reconstruct the difference between the age of the gas and of the ice at the respective depth correctly.

The firn densities in Fig. 5.8a described the same cross-section of NEGIS as the density profile that was derived from records of the seismic velocity in the firn by Riverman et al. (2019). To compare the model results with the data, Fig. 9 from Riverman et al. (2019) is adopted in this thesis as Fig. 5.9. The shape of the modelled firn density generally agrees very well with the recorded density. However, the deviation of the firn thickness in the shear margins is bigger in the recorded data, with values of around 30 m, than in the modelled firn, where a decrease by 20 m is predicted.

While the firn-ice transition in the shear margins occurs in both, the model and the data, at a depth of around 40 m, the transition in the centre and outside of the ice stream is found in the data at greater depth than it is in the model. This suggests, that the model produces accurate results at high strain rates, but overestimates the firn densification

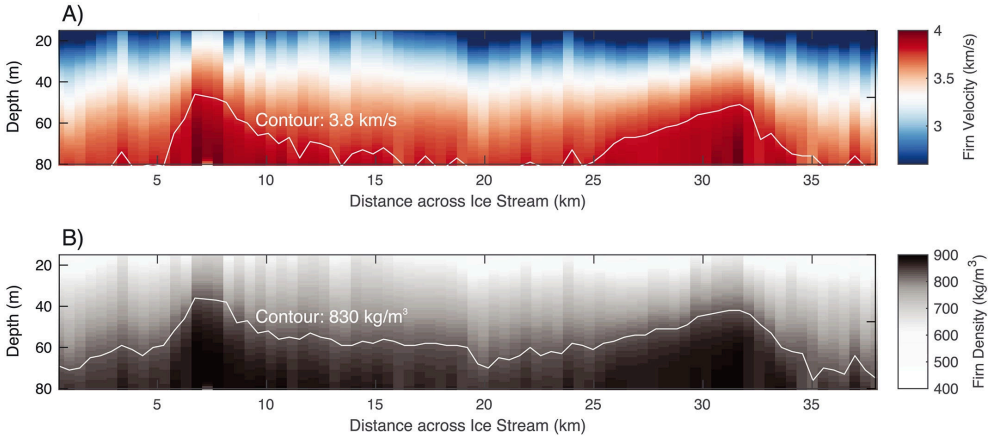

Figure 5.9.: (a) Seismic velocity recorded along a cross-section of NEGIS. (b) Firn density that was inferred from (a) by calibration with the NEGIS firn core. The white contour line indicates the firn-ice transition. Adopted with permission from Riverman et al. (Fig. 9, 2019).

rate, when strain rates are small. Nonetheless, the results demonstrate that in general the decreased firn thickness in the shear margins can be reproduced well, when the effect of strain softening due to the horizontal strain rates is considered.

5.3.3. Radar surveys

As a next step, the significance of horizontal strain rates for the interpretation of radar data is examined. In Fig. 5.10 the radargram from EGRIP towards the South-East shear margin, that was presented in Section 4.2.2, is shown. The longest two-way traveltimes in this plot correspond to a depth of around 40 m. Additional to the radargram the contour lines for certain ages of two synthetically produced radargrams are shown.

The synthetic radargrams are created by modelling the firn at the original radar line with and without considering the impact of the horizontal strain rates. The firn densities are transferred into two-way travel times, following the method described in Appendix A.2. The accumulation his-

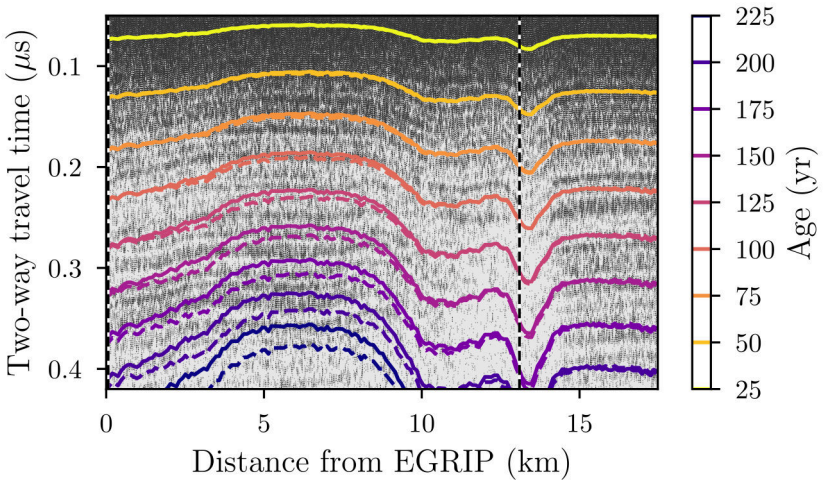

Figure 5.10.: Radargram recorded from EGRIP across the South-East shear margin. The same section is reproduce by two synthetic radargrams, where one was created with the classical Herron-Langway model (dashed contour lines) and one with the extension for strain softening and pure shear (solid contour lines). The radar data was recorded by (D. A. Lilien et al, unpublished, 2020).

tory for EGRIP is employed and scaled at every location according to the radar derived accumulation rates, which were shown in Fig. 4.3. The synthetic radargrams allow to study the effect of horizontal strain rates on radar observations, because for them all relevant quantities, which are the depth, density, age and the two-way travel time are known.

At small traveltimes and firn ages and also in the shear margin, which is located at a distance of approximately 12 to 15 km from EGRIP, both models agree well with each other and with the recorded radargram. This reinforces the properness of the accumulation rates that were derived from the 44 yr-layer of the original radargram, but also illustrates that strain softening does not strongly affect the two-way travel time and hence radar observations in general.

In the interior of the ice stream on the other hand, larger deviations between the two artificial radargrams can be seen and also the agreement with the data is lower. This first tells, that the accumulation rate for this section of the ice stream must have varied considerably in the past and second, that another strain-based effect must have a significant impact on the two-way travel time. When accumulation rates are inferred from the radargram at great depth, this effect needs to be considered in order to avoid potentially faulty estimates of the past accumulation rate.

Before taking a closer look at the deviations in the interior of the ice stream, the effect of strain-softening is studied in more detail. Radar surveys are often conducted in order to determine the ice thickness. A decreased firn thickness however would induce a bias into the depth estimate, when it is not considered in the reconstruction of the depth from the two-way travel time, because of a lower propagation velocity of the radar wave in dense firn.

This depth error can be estimate from the two synthetic radargrams, because for every point of the derived travel time the input depth is known. Accordingly, the depth estimate that both models would predict for a specific travel time can be compared with each other. When the depth of the strain-based model is regarded as the true value, then the

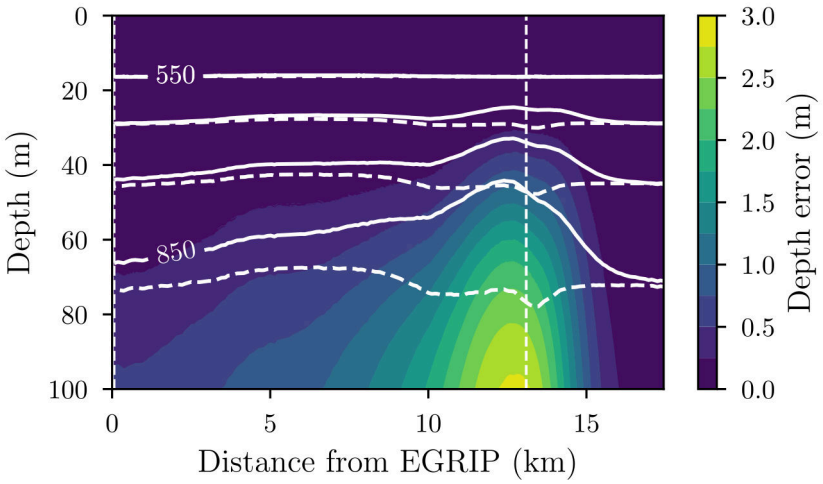

Figure 5.11.: Error of the depth estimate in the South-East shear margin of NEGIS, when the impact of strain softening is not considered in the reconstruction of the depth from the two-way travel time. The white contours indicate the depth of the corresponding density according to the classical (dashed line) and strain-based (solid line) densification model.

difference of the depth estimate of the classical model conforms exactly to the depth error that would be induced, when the enhanced firn density by strain softening is neglected in the reconstruction of depth from the two-way travel time.

The computed error of the depth estimate is displayed in Fig. 5.11. The plot shows that in the shear margins the depth of a specific layer at the bottom of the firn column will be overestimated by up to 3 m, when strain softening is not considered. This corresponds to about 10 % of the decrease of the firn thickness. As the depth estimate of all lower layers will possess the same error, the total thickness of the ice sheet is also overestimated by 3 m.

To understand why the synthetic radargrams distinguish stronger in the interior of the ice stream than in the shear margins, the general impact of horizontal strain rates on the two-way travel time is studied. The time that a radar wave needs to propagate through a specific layer

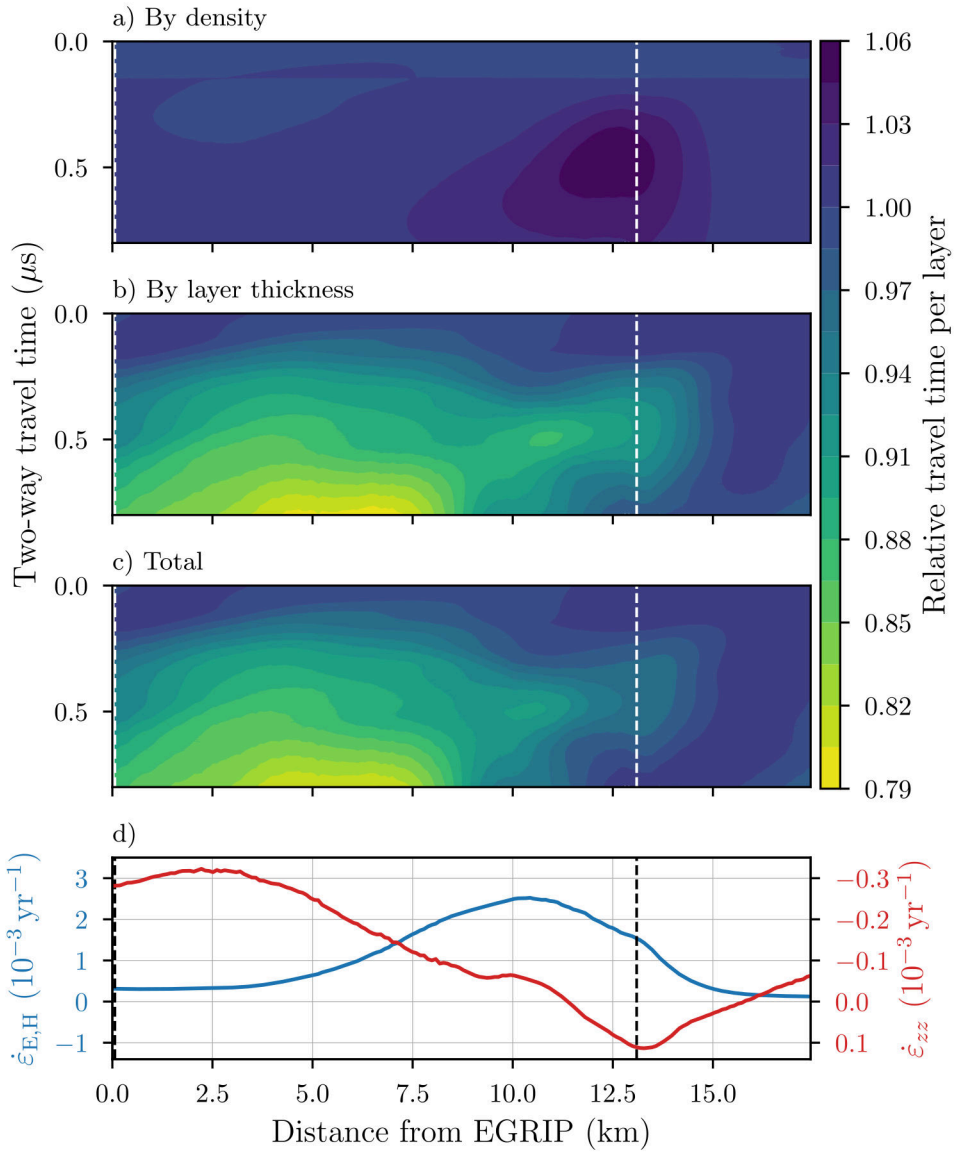

Figure 5.12.: Relative change of the two-way travel time per layer by (a) an increased firn density, (b) a decreased layer thickness and (c) in total. (d) Mean effective horizontal strain rate and vertical strain rate by pure shear along the radar line over the age of the oldest layer. The vertical, dashed line indicates the location of the EGRIP S5 2019 firn core.

depends on two parameters, the layer thickness and the density. While strain softening affects both, by compacting and thinning the firn layers. Pure shear only changes the layer thickness.

As the depth and density of every layer are known for the synthetic radargrams, it is possible to determine, how the travel time in every layer changes by the two effects in the strain-based model. The results are depicted in Fig. 5.12. The travel time of a radar wave in the firn is generally affected much stronger by the thinning of the individual layers than by the change of the density. The increase of the travel time due to the enhanced density in the shear margins is superimposed by the counteracting effect of layer thinning. The two synthetic radargrams distinguish most, where the layer thickness has changed the strongest.

Figure 5.12d shows the mean effective horizontal strain rate, which is associated with strain softening, and the mean vertical strain rate, that is induced by pure shear. The change of the travel time by the density in Fig. 5.12a corresponds to the effective horizontal strain rate, which however also induces counteracting layer thinning. On the contrary, the vertical strain rate only correlates with the strong change of the layer thickness in the centre of the ice stream, which confirms that the strong deviation between the two synthetic radargrams in the interior of the ice stream are caused by pure shear. Consequently, for the correct interpretation of radar data it is more important to consider pure shear than strain softening, despite the much larger magnitude of the effective horizontal strain rate.

The stretching of the firn that is observed here can be associated with a bump in the surface topography that can be seen upstream of the radar line (Vallelonga et al., 2014), where the firn is dragged downhill. This bump likely also causes the variability of the past accumulation rate in the centre of the ice stream that Fig. 5.10 shows.

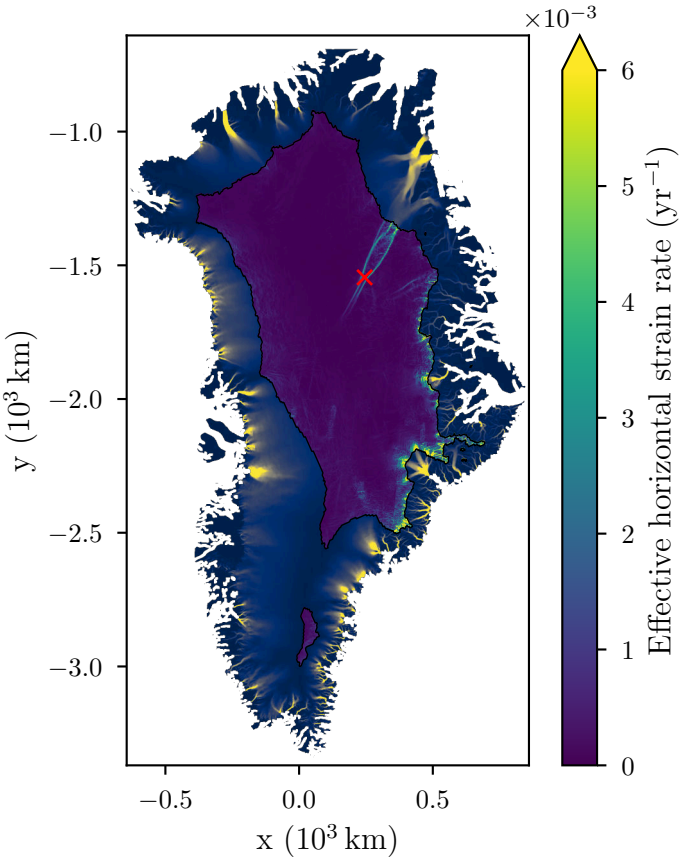

Figure 5.13.: Effective horizontal strain rate in the GrIS low-melt zone. The background shows the ice flow velocity from Joughin et al. (2016).

5.4. GrIS firn air content

As a last step, the model is used to estimate the change of the firn air content of the Greenland ice sheet due to horizontal strain rates. Therefore, the effective horizontal strain rate is determined for the zone of the GrIS with on average less than 1 mm of melt per year in the HIRHAM5 RCM output. High melt rates are excluded, because they are expected to strongly affect firn densification by water percolation and refreezing, which is not included in the strain softening model. The effective horizontal strain rates that are present in this low-melt zone are

shown in Fig. 5.13. The figure demonstrates the uniqueness of NEGIS, because it is the only region on Greenland, where high horizontal strain rates are observed in the interior of the ice sheet. Nevertheless, high strain rates at dry conditions are also present at the onset of the big outlet glaciers in South-East Greenland.

Combining the effective horizontal strain rate with the multi-year means of the temperature and the accumulation rate of the HIRHAM5 output, the firn properties at every grid point can be approximated. The DIP, BCO depth and BCO age are determined by interpolating the forcing parameters onto the parameter grids that were created in Section 5.1 by modelling the firn with steady-state conditions for variable forcing parameters.

The resulting maps of the DIP, BCO depth and BCO age, as well as their respective changes compared to a model without strain, are shown in Fig. 5.14. The DIP always corresponds to about one third of the BCO depth, so that the maps of both quantities resemble each other strongly. They confirm the results from Fig. 5.1 that both quantities mainly scale with the strain rate. Hence they can be estimated in good approximation directly from a map of the effective horizontal strain rate. The map of the BCO age shows that large deviations of the firn age at the firn-ice transition only occur at NEGIS, where the firn is generally old due to low temperatures and low accumulation rates. At other locations on Greenland the influence of strain rates is less important for the interpretation of ice core records.

From the change of the DIP, the additional mass in the GrIS due to the denser firn in regions of high horizontal strain rates can be determined. Integrating the DIP over the whole area of little melt, this results in $489\,\mathrm{km}^3$ or $449\,\mathrm{Gt}$ of additional ice in the GrIS, which are not captured when the firn air content is estimated with a classical models. Transferring this ice mass into sea-level equivalents gives a value of $1.24\,\mathrm{mm}$, which is negligible compared to the $7.3\,\mathrm{m}$ of the Greenland ice sheet (Cuffey and Paterson, 2010).

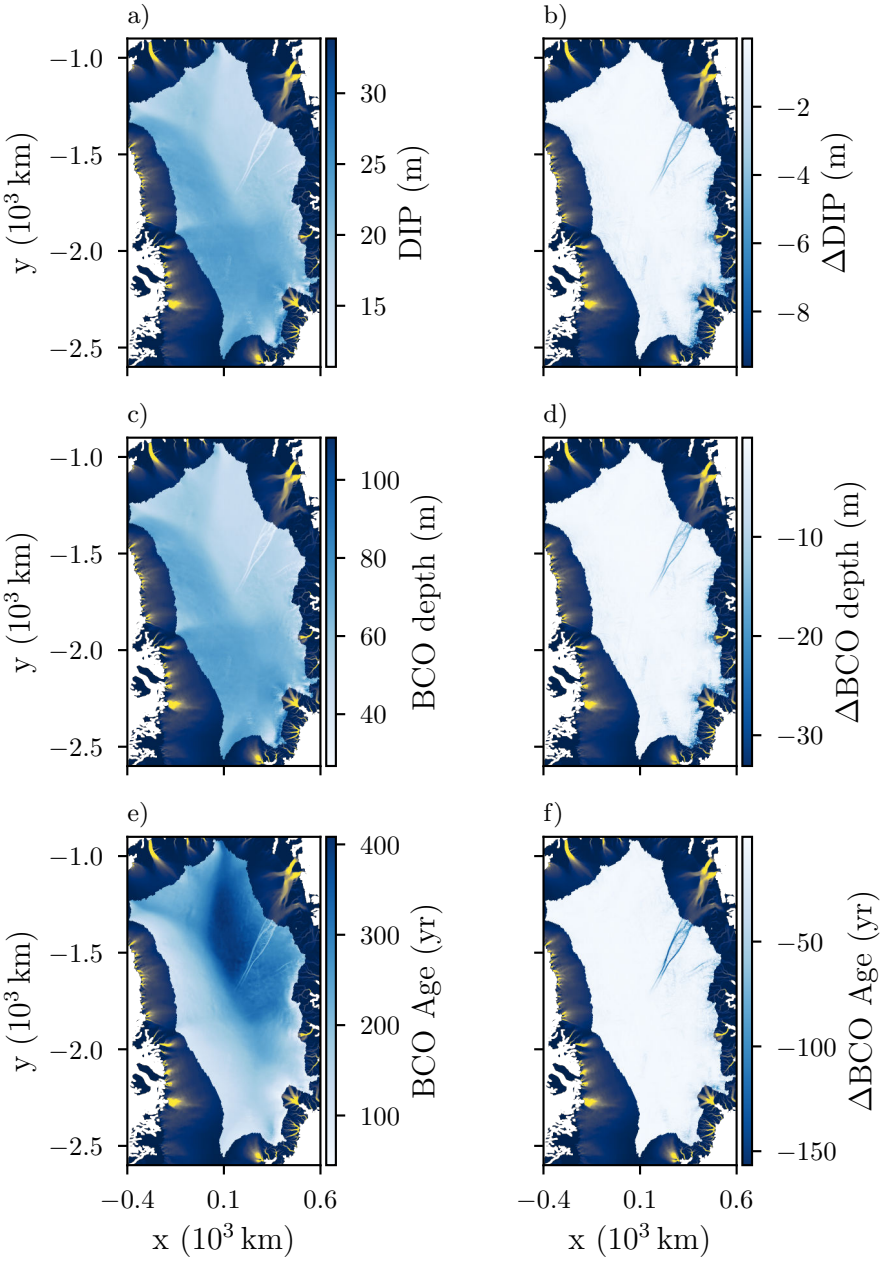

Figure 5.14.: Maps of the GrIS low-melt zone of (a) the DIP and (b) its change due to strain softening, (c) the BCO depth and (d) its change and (e) the BCO age and (f) its change. All quantities are inferred from the interpolation of the local forcing parameters onto the results of the sensitivity tests.

6. Discussion

Densification in the shear margins

Different processes that affect the densification of polar firn in regions with high horizontal strain rates were modelled in order to evaluate their potential contribution to the enhanced firn densification, that can be observed in the shear margins of ice streams. Strain softening was identified as the dominant mechanism, as previous studies have suggested (Alley and Bentley, 1988; Riverman et al., 2019). Pure shear, which was proposed by Fahnestock et al. (2001) as the cause of the shear margins troughs, could be ruled out as the driving mechanism. Locally pure shear can strongly affect the firn thickness, but it does not obey a spatial pattern that allows the creation of shear margin troughs (Fig. 4.1g). At locations where the firn is horizontally compressed, it can even increase the firn thickness and the surface elevation in the shear margins.

In principle, horizontal strain rates can not only affect the firn densification in the shear margins directly, but also indirectly by changing the firn temperature. The effects of strain heating and vertical heat flow (Holschuh et al., 2019) were modelled, but in comparison with strain softening both effects proved to be of minor importance, if not negligible. To affect firn compaction considerably, the vertical flow of heat would need to raise the firn temperature by about 6 °C, which is the maximum increase of the depth-averaged temperature by vertical heat flow that Holschuh et al. (2019) detected in the shear margins. However, as the firn is consistently cooled from the surface, the change of temperature is likely lower in the firn. Accordingly, this study indicates that

temperature variations in the shear margins do not significantly contribute to the enhanced firn densification rate. As the effective activation energy of the Herron-Langway model is doubled in the load-based formulation, the low temperature sensitivity of the Herron-Langway model should also not compromise these results. Nonetheless, direct measurements of the temperature are needed to validate this assumption and to ascertain the impact of the temperature variations more precisely.

The increase of the accumulation rate in the shear margins troughs is also too small to affect the firn thickness considerably, compared to the thinning by strain softening (Fig. 5.6). Consequently, neither other strain-based densification mechanisms nor the deviations of the temperature and accumulation rate can explain the reduced firn thickness in the shear margins. With the developed model for strain softening, however, this feature can be reproduced as the comparison of the modelled firn density cross-section of NEGIS with recorded data by Riverman et al. (2019) demonstrates. This indicates that firn densification in the presence of high horizontal strain rates is dominated by strain softening.

The modelled reduction of the firn thickness conforms to the lowered surface elevation in the shear margins of NEGIS. Hence, it is suggested that the shear margin troughs are formed due to strain softening. Their formation can thereby be imagined as a collapse of the firn, caused by the reduced viscosity. As the shear margin troughs are the most pronounced features of an ice stream, they are expected to contribute significantly to its stability, for example by changing the subglacial hydropotential (Riverman et al., 2019). Therefore, the results indicate that the dynamics of ice streams cannot be understood without considering the effect of strain softening on the densification of firn. Examining the dynamics of ice streams and the formation of shear margins troughs in more detail would exceed the scope of this thesis, but the developed model can act as a starting point for studying these processes.

model performance at low strain rates

While in the shear margins the performance of the model is satisfying, it is less accurate in the centre and outside of the ice stream, where horizontal strain rates are small. In comparison to both, firn core data (Fig. 5.6) and a density reconstruction from seismic velocities (Figs. 5.8d and 5.9b), the Herron-Langway model with the extension for strain softening overestimates the reduction of the firn thickness by approximately 10 m. At these locations the effective horizontal strain rate has a value of around $3 \times 10^{-4}\,\mathrm{yr}^{-1}$. This overestimation is related to a strong sensitivity of the model to low horizontal strain rates (Fig. 5.2). Accordingly the discrepancy can be explained in two ways, either the model is too sensitive in the presented formulation or the classical Herron-Langway model already implicitly regards a small contribution of strain softening to the densification rate, so that the developed model considers the effect twice.

Because the model for strain softening was derived directly from well-established physical relations, the sensitivity is expected to be accurate. It is however likely that the Herron-Langway model incorporates a bias. As Figs. 4.1g and 5.14 show, small strain rates can be observed at many locations on the ice sheet and therefore likely also occurred at the sites of the firn cores that were used to tune the model. The assumption is supported further by the median of the derived effective horizontal strain rates of the GrIS, which amounts to $4 \times 10^{-4}\,\mathrm{yr}^{-1}$. Hence, at least some of the firn cores that were used to tune the Herron-Langway model were likely subjected to horizontal strain rates. Accordingly, the effect of moderate strain softening is probably incorporated in the empirically tuned model parameters. The performance of the model at high strain rates is affected less by the bias, because at high strain, the sensitivity of the model to variations of the strain rate is generally lower.

Simonsen et al. (2013) noted that firn compaction cannot sufficiently be parametrised only by the temperature and accumulation rate. The findings suggest that the impact of horizontal strain rates on firn dens-

ification is considerable, not only in the high-strain shear margins, but on the whole ice sheet. Establishing it as a third forcing parameter can thus potentially increase the general accuracy of firn densification models. Furthermore, the approach of the model underlines the potential of modelling firn densification solely based on the viscosity and load, as done in the Crocus model (Vionnet et al., 2012), which can be taken as a basis for the development of an entirely physics-based firn densification model.

Validation of the model

Even though the observed firn density in the shear margins could be reproduced appropriately with the developed model, additional validation data is required to assess its accuracy in more detail. In particular, a comparison of the model with data from a shear margin firn core or with directly measured densification rates from an ApRES instrument (Nicholls et al., 2015) can be useful, in order to examine the performance of the model at every depth.

In this thesis, it is assumed that strain softening solely affects the second stage of firn densification, where power-law creep is dominant, but in reality the transition from grain-boundary sliding to power-law creep as the dominant densification mechanism is expected to be smooth and in a certain density region the contribution of both mechanisms is likely significant at the same time. So far, the density range of this transition is not conclusively ascertained (Maeno and Ebinuma, 1983; Ebinuma and Maeno, 1987; Wilkinson, 1988). Because strain softening only affects power-law creep, but not grain-boundary sliding, adapting the model to the data can not only improve the accuracy of the model, but potentially also help to gauge the transition region better.

In theory, strain softening can moreover shift the critical density towards lower values. Arnaud et al. (1998) have suggested that at low temperatures the load at a fixed density is increased, so that power-law

creep is enhanced and thereby the critical density is shifted towards lower values. For strain softening a similar behaviour can be anticipated, which however needs to be confirmed by firn core data.

Further research is also needed to examine the range of applicability of the model. At low temperatures other densification mechanisms like lattice diffusion and grain boundary diffusion are expected to become important, whereby strain softening might affect the densification rate less strongly. Strain softening can possibly also be affected by the occurrence of percolating meltwater and ice lenses. As horizontal strain rates are especially high along the fast-flowing outlet glaciers, which often initiate in the percolation zone, the interaction between the two effects can potentially be relevant.

Impact on radar surveys

With the model for strain softening synthetic radargrams for the shear margins of NEGIS were created. They allow to study how alterations in the firn by horizontal strain rates influence the outcome of radar surveys. Two potential error sources were identified. The travel time of a radar wave through a specific firn layer can be lowered by both strain softening and pure shear, whereat the latter proved to be of higher importance for the estimation of past accumulation rates from radargrams, because for strain softening the effect of an increased firn density almost balances the reduced layer thickness.

As the propagation time is more sensitive to the depth than to the density, the bias of the depth estimate by strain softening of 3 m even in the highly strained shear margins is low compared to the firn thickness and especially to the dimensions of an ice sheet and to variations in bedrock topography. Hence, this error can be neglected for most applications, however, can also easily be considered by applying the presented model.

On the contrary, the impact of pure shear, which refers to a compression or stretching of the firn column and is caused by an imbalance between the two principal horizontal strain rates, needs to be considered for the determination of past accumulation rates from radargrams. The thinning by a moderate vertical strain rate of around $3 \times 10^{-4}\,\mathrm{yr}^{-1}$ can cumulate over time and reduce the layer thickness at the bottom of the firn column by 20 %. If not considered, the error of the estimated accumulation rate would be of the same order.

Firn properties of the GrIS

According to the forcing by the HIRHAM5 RCM output (Langen et al., 2017; Mottram et al., 2017) and to the horizontal strain rates derived from the Ice Sheet Velocity Mosaic (Joughin et al., 2016), the DIP and the BCO age and depth for the low-melt zone of the GrIS were approximated with the model. The integration of the change of the DIP by strain softening over the ice sheet revealed an additional ice mass that corresponds to 1.24 mm of sea-level equivalent, which approximately conforms to the annual mass loss of the ice sheet, but is negligible compared to its total mass. Considering the underestimation of the firn thickness at low strain rates, the change of the total DIP will even be overestimated by the model and hence, the additional mass will in fact be lower. Accordingly, it is not crucial to consider the effect of strain softening for the estimation of the total firn air content of an ice sheet. Nevertheless, it might be locally important in the study of high-strain regions and also for the estimation of the annual mass balance from radar altimetry, because if ice streams and outlet glaciers accelerated due to climate change, the horizontal strain rates and thereby the general densification of the firn by strain softening would increase, which would then lower the surface elevation. Hence, it is suggested to consider horizontal strain rates for estimating the mass balance, because classical densification model would not capture this effect.

The map of the change of BCO age in Fig. 5.14f revealed another unique feature of NEGIS. Because of a generally high BCO age in North-East Greenland, its change by horizontal strain is particularly high along the shear margins of NEGIS. Figure 5.8d shows that the firn BCO age and therefore also the Δage between the gas and ice record, is lowered by 200 yr or 50 % in the shear margins. This shift does not only need to be considered in the interpretation of the chronologies of the gas and isotope records of the deep EGRIP ice core at the time where the ice passed the shear margin, but also suggests that these special conditions, together with the also lower BCO depth, can possibly be exploited as a natural laboratory for the studies of firn air diffusion. The climatic conditions within the shear margins are very similar to the conditions outside, whereas inside gas inclusion proceeds much faster and at shallower depth. This feature can potentially be used to ascertain the contributions and time scales of the different sub-processes, like gravitational fractionation and isotopic diffusive fractionation (Buizert, 2013), more precisely.

7. Conclusion

A model for the enhanced firn densification in the presence of horizontal strain rates by the effect of strain softening was developed. It has been implemented as an optional module in the framework of the Community Firn Model (Stevens et al., 2020) and can be employed with any of the included classical firn densification models.

This model in particular allows for the first time to accurately model the process of firn densification in the shear margins of an ice stream. It thereby enables to compare the effect of strain softening with other processes that can affect the densification of firn that is subjected to horizontal strain rates. These tests confirmed that strain softening is distinctly the driving mechanism for the increased firn densification that has been observed in the shear margins of ice streams, as suggested by previous studies (Alley and Bentley, 1988; Riverman et al., 2019).

The reduction of the firn thickness correlates well with the location and magnitude of the shear margin troughs, which indicates that their formation is caused by strain softening. Accordingly, the presented model is likely a key component of an complete ice stream model. Thereby, it can contribute to the assessment of the stability of ice streams, which is crucial for the estimation of their potential contribution to future sea-level rise under a changing climate.

Furthermore, the model can be used in the interpretation of radar data, where the effect of horizontal strain rates on the firn structure, if it is not considered, induces a bias in the estimate of the depth and of the past accumulation rate. Another field of application lies in the correction of the mass balance estimate from radar altimetry, because strain softening

in the firn can potentially affect the surface elevation, if ice streams and outlet glacier accelerate due to climate change. The model will moreover be useful for the interpretation of the chronologies of the gas and isotope records of the deep EGRIP ice core, because the age difference between the two will be lowered due to strain softening at the point where the ice has passed the shear margin.

Eventually, this study gives implications for the development of a physics-based firn densification model. It demonstrates the potential of modelling firn densification solely based on the viscosity and load. The high sensitivity of the model to low strain rates further suggests, that besides the temperature and accumulation rate, the effective horizontal strain rate is an important forcing parameter for the densification of firn. In particular, because horizontal strain rates occur at many locations on the ice sheet, strain softening by moderate horizontal strain rates is likely already considered implicitly in the empirically tuned parameters of the Herron-Langway model and other classical firn densification models. Considering the effective horizontal strain rate explicitly as a third forcing parameter can thus in any case improve the general accuracy of firn densification models.

A. Appendix

A.1. Residual strain rate

The vertical strain rate that is associated with the thinning of firn and ice layers due to the flow of ice towards the margins of an ice sheet can be estimated, when the past accumulation rate and the age and depth of two layers in the ice are known at a specific location from for example an ice core.

The thickness of an annual layer with an age t in years is given by

$$\lambda_t = \lambda_0 \dot{\varepsilon}_{zz} t, \tag{A.1}$$

where $\dot{\varepsilon}_{zz}$ is the vertical strain rate by ice flow and λ_0 is the initial layer thickness, which corresponds to the mean accumulation rate in meters of ice equivalent. Therefore, the depth of an annual layer z_n with age t_n can be approximated by the sum of the thickness of all annual layers above, which is given by

$$z_n(t_n) = \sum_{t=1}^{t_n} \lambda_0 \dot{\varepsilon}_{zz} t. \tag{A.2}$$

This equation, however, entails a bias, because the porous firn is neglected. To correct for this bias, two layers that have attained the density of ice can be subtracted from each other, before solving the equation for $\dot{\varepsilon}_{zz}$, which gives

$$\dot{\varepsilon}_{zz} = \frac{z_1 - z_2}{\lambda_0 \sum_{t=t_1}^{t_2} t}, \tag{A.3}$$

where the subscripts 1 and 2 refer to the upper, respectively lower layer.

From the NEEM ice core (Rasmussen et al., 2013), the layers at a depth of 111.16 m and 1 003.42 m with an age of 400 yr and 6 000 yr can be taken. As both layers were formed in the Holocene, the accumulation rate remained almost constant in the meantime with a mean value of $0.227\,\mathrm{m.\,i.e.\,yr^{-1}}$. Inserting these values into Eq. (A.3) gives a vertical strain rate of $-2.2 \times 10^{-4}\,\mathrm{yr^{-1}}$.

A similar approximation could be made with data from the EGRIP ice core, but as the drill site lies in a fast flowing ice stream, the accumulation rate changed considerably in the Holocene, because of higher accumulation rates upstream (Mojtabavi et al., 2019). Thus, the vertical strain rate would be underestimated. Nonetheless, a value of $-1.7 \times 10^{-4}\,\mathrm{yr^{-1}}$ can be obtained for EGRIP, which suggests that the vertical strain rate by ice flow does not change considerably over the ice sheet and that a value of $-2 \times 10^{-4}\,\mathrm{yr^{-1}}$ is a good approximation for the residual strain rate.

A.2. Two-way travel time

The two-way travel time is modelled in this thesis following (Karlsson et al., 2020). The permittivity ε' of a layer at depth z is assumed to scale with the firn density ρ according to the Looyenga mixing model (Looyenga, 1965) given by

$$\varepsilon'(z) = \left(\frac{\rho(z)}{\rho_\mathrm{i}} \left[\sqrt[3]{\varepsilon'_\mathrm{i}} - 1 \right] + 1 \right)^3, \tag{A.4}$$

where $\rho_\mathrm{i} = 917\,\mathrm{kg\,m^{-3}}$ and $\varepsilon'_\mathrm{i} = 3.15$ are the density and permittivity of ice. The velocity of the radar wave in turn is given by the velocity of light c_0, scaled with the permittivity by

$$v(z) = \frac{c_0}{\sqrt{\varepsilon'(z)}}, \tag{A.5}$$

with that the two-way travel time can simply be computed at every depth by

$$\tau(z) = \int_0^z \frac{2}{v(z')} dz'. \tag{A.6}$$

A.3. Implementation of the strain-modules

A.3.1. Initialisation

```
if self.c['strain']:
    input_eps_1, input_eps_2, input_year_eps = read_input2
   (os.path.join(self.c['InputFileFolder'],self.c['
   InputFileNameStrain']))
    d1sf = interpolate.interp1d(input_year_eps,input_eps_1
   ,int_type,fill_value='extrapolate')
    d2sf = interpolate.interp1d(input_year_eps,input_eps_2
   ,int_type,fill_value='extrapolate')
    self.eps_1   = d1sf(self.modeltime)
    self.eps_2   = d2sf(self.modeltime)
    self.eps_EH2 = (self.eps_1 ** 2 + self.eps_2 ** 2) / 2
    self.eps_zz  = - (self.eps_1 + self.eps_2)  # 1/yr
    self.eps_zzSec = self.eps_zz / S_PER_YEAR   # 1/s
else:
    if 'strain_softening' in self.c:
        if self.c['strain_softening']:
            self.c['strain_softening']=False
            print("To model strain softening, you need to
   turn strain on.")
    if 'strain_heating' in self.c:
        if self.c['strain_heating']:
            self.c['strain_heating']=False
            print("To model strain heating, you need to
   turn strain on.")
```

The modules for `strain_softening` and `strain_heating` are initialised together with the already implemented `strain`-module for pure shear at the beginning of the spin-up and main run. If strain is activated,

the input files are loaded and interpolated onto the model time steps. The input file is expected to contain two rows that give the principle horizontal strain rates, instead of one row that only gives the vertical strain rate by pure shear, which was originally used. Subsequently, the effective horizontal strain rate `eps_EH2` and the vertical strain rate by pure shear `eps_zz` are computed. If strain is not activated, but the modules for strain softening and heating are, then they also do not work and are deactivated. The existence of the configuration keys for the implemented modules is checked before, so that the code works also if they are not included in the configuration file.

A.3.2. Execution

```
if self.c['strain']:
    eps_zz_c = - drho_dt / self.rho * S_PER_YEAR
    if 'residual_strain' in self.c:
        eps_zz_c = eps_zz_c - np.abs(self.c['
   residual_strain'])
    else:
        eps_zz_c = eps_zz_c - 2e-4

    if 'strain_softening' in self.c:
        if self.c['strain_softening']:
            strain_Ec2 = 0.5 * (eps_zz_c ** 2)
            rH2 = self.eps_EH2[iii] / eps_E_c2
            K = (13.5 * r_hor2 + 1.5 * np.sqrt(81 * rH2 **
    2 + 12 * rH2) + 1) ** (1 / 3)
            rV = (K + 1 / K + 1) / 3
            z2mask = (self.rho >= RHO_1)
            drho_dt[z2mask] = drho_dt[z2mask] * rV[z2mask]
            self.viscosity[z2mask] = self.viscosity[z2mask
   ] / rV[z2mask]
            eps_zz_c[z2mask] = eps_zz_c[z2mask] * rV[
   z2mask]

    if 'strain_heating' in self.c:
```

```
20          if self.c['strain_heating']:
21              self.eps_tr = eps_zz_c
22              self.eps_E2 = 0.5 * (self.eps_1[iii]**2 + self
    .eps_2[iii]**2 + (eps_zz_c + eps_zz)**2)
23
24      self.dz     = (1 + self.eps_zzSec[iii] * self.dt[iii])
        * self.dz    # Pure shear
25      self.mass   = (1 + self.eps_zzSec[iii] * self.dt[iii])
        * self.mass  # Pure shear
```

The strain rate modules are executed at each time step (`iii`) directly after the densification rate `drho_dt` has been determined with a classical firn model. The vertical strain rate of the classical model `eps_zz_c` is computed following Eq. (3.9). With the `residual_strain`-key the residual strain rate for the regularisation can be set, otherwise the value of $-2 \times 10^{-4}\,\mathrm{yr}^{-1}$, derived in Appendix A.1 is applied.

Subsequently, if active, `strain_softening` is executed by computing `rV`, following Eqs. (3.18) and (3.23) to (3.27), and accordingly correcting the densification rate, the corresponding vertical strain rate and the viscosity that are given by the classical model. The correction is only applied in the second stage, indicated by `z2mask`, but in principle can easily be activated in the first stage.

`strain_heating` is executed separately in the core module for heat diffusion, but two variables that are needed for the later computation of the source term for strain heating are already computed, which are the trace `eps_tr` and the squared effective strain rate `eps_E2` of the full strain rate tensor. Note that the trace is only given by the, potentially corrected, vertical strain rate from the densification of the firn.

When the `strain`-module is turned on, the computations for pure shear are always executed in the end, in which the mass and the thickness of each layer are scaled according to the vertical strain rate by pure shear, see Eq. (3.13), as implemented before.

A.3.3. Execution – Strain heating

```
S_eps_heat = 0
if 'strain_heating' in self.c:
    if self.c['strain_heating']:
        S_eps_heat = 4 * self.viscosity * self.eps_E2 /
   S_PER_YEAR**2
        S_eps_heat = S_eps_heat - self.eps_tr * self.sigma
    / S_PER_YEAR

self.Tz = transient_solve_TR(z_edges_vec, z_P_vec, nt,
   self.dt[iii], Gamma_P, phi_0, nz_P, nz_fv, phi_s,
   tot_rho, c_vol, S_C=S_eps_heat)
```

The module for `strain_heating` is eventually executed in the core module for heat diffusion. Before the solver for the heat diffusion equation (3.7) is called, the source term for strain heating `S_eps_heat` is computed according to Eq. (3.30) and passed as an optional argument to the solver. If strain heating is not considered, the source term is set to zero.

Bibliography

Alexander, P. M., Tedesco, M., Koenig, L., and Fettweis, X. (2019). Evaluating a regional climate model simulation of Greenland ice sheet snow and firn density for improved surface mass balance estimates. *Geophysical Research Letters*, 46(21):12073–12082.

Alley, R. B. (1987). Firn densification by grain-boundary sliding: A first model. *Journal de Physique Colloques*, 48(C1):C1–249–C1–256.

Alley, R. B. and Bentley, C. R. (1988). Ice-core analysis on the Siple Coast of West Antarctica. *Annals of Glaciology*, 11:1–7.

Arnaud, L., Barnola, J. M., and Duval, P. (2000). Physical modeling of the densification of snow/firn and ice in the upper part of polar ice sheets. In *Physics of ice core records*, pages 285–305. Hokkaido University Press.

Arnaud, L., Lipenkov, V., Barnola, J. M., Gay, M., and Duval, P. (1998). Modelling of the densification of polar firn: Characterization of the snow–firn transition. *Annals of Glaciology*, 26:39–44.

Arthern, R. J., Vaughan, D. G., Rankin, A. M., Mulvaney, R., and Thomas, E. R. (2010). In situ measurements of Antarctic snow compaction compared with predictions of models. *Journal of Geophysical Research: Earth Surface*, 115(F3).

Bader, H. (1954). Sorge's law of densification of snow on high polar glaciers. *Journal of Glaciology*, 2(15):319–323.

Bentsen, M., Bethke, I., Debernard, J. B., Iversen, T., Kirkevåg, A., Seland, Ø., Drange, H., Roelandt, C., Seierstad, I. A., Hoose, C., and Kristjánsson, J. E. (2013). The Norwegian Earth System Model, NorESM1-M – Part 1: Description and basic evaluation of the physical climate. *Geoscientific Model Development*, 6(3):687–720.

Braithwaite, R. J., Laternser, M., and Pfeffer, W. T. (1994). Variations of near-surface firn density in the lower accumulation area of the Greenland ice sheet, Pâkitsoq, West Greenland. *Journal of Glaciology*, 40(136):477–485.

Brun, E., David, P., Sudul, M., and Brunot, G. (1992). A numerical model to simulate snow-cover stratigraphy for operational avalanche forecasting. *Journal of Glaciology*, 38(128):13–22.

Buizert, C. (2013). Ice core methods | Studies of firn air. In *Encyclopedia of Quaternary Science*, pages 361–372. Elsevier, 2nd edition.

Buizert, C., Cuffey, K. M., Severinghaus, J. P., Baggenstos, D., Fudge, T. J., Steig, E. J., Markle, B. R., Winstrup, M., Rhodes, R. H., Brook, E. J., Sowers, T. A., Clow, G. D., Cheng, H., Edwards, R. L., Sigl, M., McConnell, J. R., and Taylor, K. C. (2015). The WAIS Divide deep ice core WD2014 chronology – Part 1: Methane synchronization (68–31 ka BP) and the gas age–ice age difference. *Climate of the Past*, 11(2):153–173.

Christianson, K., Peters, L. E., Alley, R. B., Anandakrishnan, S., Jacobel, R. W., Riverman, K. L., Muto, A., and Keisling, B. A. (2014). Dilatant till facilitates ice-stream flow in northeast Greenland. *Earth and Planetary Science Letters*, 401:57–69.

Cuffey, K. M. and Paterson, W. S. B. (2010). *The Physics of Glaciers*. Elsevier, Amsterdam, etc., 4th edition.

Dee, D. P., Uppala, S. M., Simmons, A. J., Berrisford, P., Poli, P., Kobayashi, S., Andrae, U., Balmaseda, M. A., Balsamo, G., Bauer, P., Bechtold, P., Beljaars, A. C. M., van de Berg, L., Bidlot, J., Bormann, N., Delsol, C., Dragani, R., Fuentes, M., Geer, A. J., Haimberger, L., Healy, S. B., Hersbach, H., Hólm, E. V., Isaksen, L., Kållberg, P., Köhler, M., Matricardi, M., McNally, A. P., Monge-Sanz, B. M., Morcrette, J.-J., Park, B.-K., Peubey, C., de Rosnay, P., Tavolato, C., Thépaut, J.-N., and Vitart, F. (2011). The ERA-Interim reanalysis: configuration and performance of the data assimilation system. *Quarterly Journal of the Royal Meteorological Society*, 137(656):553–597.

Ebinuma, T. and Maeno, N. (1987). Particle rearrangement and dislocation creep in a snow-densification process. *Journal de Physique Colloques*, 48(C1):263–269.

Fahnestock, M. A., Joughin, I., Scambos, T. A., Kwok, R., Krabill, W. B., and Gogineni, S. (2001). Ice-stream-related patterns of ice flow in the interior of northeast Greenland. *Journal of Geophysical Research: Atmospheres*, 106(D24):34035–34045.

Fausto, R. S., Box, J. E., Vandecrux, B., Van As, D., Steffen, K., MacFerrin, M. J., Machguth, H., Colgan, W., Koenig, L. S., McGrath, D., Charalampidis, C., and Braithwaite, R. J. (2018). A snow density dataset for improving surface boundary conditions in Greenland ice sheet firn modeling. *Frontiers in Earth Science*, 6(51).

Fausto, R. S. and Van As, D. (2019). Programme for monitoring of the Greenland ice sheet (PROMICE): Automatic weather station data. GEUS. Accessed on 23.07.2019.

Fourteau, K., Gillet-Chaulet, F., Martinerie, P., and Faïn, X. (2020). A micro-mechanical model for the transformation of dry polar firn into ice using the level-set method. *Frontiers in Earth Science*, 8(101).

Glen, J. W. (1955). The creep of polycrystalline ice. *Proceedings of the Royal Society of London. Series A*, 228(1175):519–538.

Greve, R. and Blatter, H. (2009). *Dynamics of Ice Sheets and Glaciers*. Springer, Berlin, Heidelberg.

Helsen, M. M., van den Broeke, M. R., van de Wal, R. S. W., van de Berg, W. J., van Meijgaard, E., Davis, C. H., Li, Y., and Goodwin, I. (2008). Elevation changes in Antarctica mainly determined by accumulation variability. *Science*, 320(5883):1626–1629.

Herron, M. and Langway, C. (1980). Firn densification: An empirical model. *Journal of Glaciology*, 25(93):373–385.

Holschuh, N., Lilien, D. A., and Christianson, K. (2019). Thermal weakening, convergent flow, and vertical heat transport in the Northeast Greenland ice stream shear margins. *Geophysical Research Letters*, 46:8184–8193.

Hörhold, M., Kipfstuhl, S., Wilhelms, F., Freitag, J., and Frenzel, A. (2011). The densification of layered polar firn. *Journal of Geophysical Research*, 116(F01001).

Joughin, I., Smith, B. E., and Howat, I. M. (2018). A complete map of Greenland ice velocity derived from satellite data collected over 20 years. *Journal of Glaciology*, 64(243):1–11.

Joughin, I., Smith, B. E., Howat, I. M., and Scambos, T. A. (2016). MEaSUREs Multi-year Greenland Ice Sheet Velocity Mosaic, Version 1. Boulder, Colorado USA. NASA National Snow and Ice Data Center Distributed Active Archive Center. Accessed on 18.03.2020.

Karlsson, N. B., Razik, S., Hörhold, M., Winter, A., Steinhage, D., Binder, T., and Eisen, O. (2020). Surface accumulation in Northern Central Greenland during the last 300 years. *Annals of Glaciology*, pages 1–11.

Langen, P. L., Fausto, R. S., Vandecrux, B., Mottram, R. H., and Box, J. E. (2017). Liquid water flow and retention on the Greenland ice sheet in the regional climate model HIRHAM5: Local and large-scale impacts. *Frontiers in Earth Science*, 4(110).

Lautrup, B. (2011). *Physics of Continuous Matter*. CRC Press, Boca Raton, Fla., 2nd edition.

Li, J. and Zwally, H. J. (2004). Modeling the density variation in the shallow firn layer. *Annals of Glaciology*, 38:309–313.

Looyenga, H. (1965). Dielectric constants of heterogeneous mixtures. *Physica*, 31(3):401–406.

Lundin, J. M. D., Stevens, C. M., Arthern, R., Buizert, C., Orsi, A., Ligtenberg, S. R. M., Simonsen, S. B., Cummings, E., Essery, R., Leahy, W., Harris, P., Helsen, M. M., and Waddington, E. D. (2017). Firn Model Intercomparison Experiment (FirnMICE). *Journal of Glaciology*, 63(239):266–281.

Maeno, N. and Ebinuma, T. (1983). Pressure sintering of ice and its implication to the densification of snow at polar glaciers and ice sheets. *Journal of Physical Chemistry*, 87(21):4103–4110.

Mojtabavi, S., Wilhelms, F., Cook, E., Davies, S., Sinnl, G., Jensen, M. S., Dahl-Jensen, D., Svensson, A., Vinther, B., Kipfstuhl, S., Jones, G., Karlsson, N. B., Faria, S. H., Gkinis, V., Kjær, H., Erhardt, T., Berben, S. M. P., Nisancioglu, K. H., Koldtoft, I., and Rasmussen, S. O. (2019). A first chronology for the East GReenland Ice-core Project (EGRIP) over the Holocene and last glacial termination. *Climate of the Past Discussions*. In review.

Morris, E. M. and Wingham, D. J. (2014). Densification of polar snow: Measurements, modeling, and implications for altimetry. *Journal of Geophysical Research: Earth Surface*, 119(2):349–365.

Mottram, R., Boberg, F., Langen, P., Yang, S., Rodehacke, C., Christensen, J. H., and Madsen, M. S. (2017). Surface mass balance of the Greenland ice sheet in the regional climate model HIRHAM5: Present state and future prospects. *Low Temperature Science*, 75:105–115.

Nicholls, K. W., Corr, H. F. J., Stewart, C. L., Lok, L. B., Brennan, P. V., and Vaughan, D. G. (2015). A ground-based radar for measuring vertical strain rates and time-varying basal melt rates in ice sheets and shelves. *Journal of Glaciology*, 61(230):1079–1087.

Nye, J. F. (1957). The distribution of stress and velocity in glaciers and ice-sheets. *Proceedings of the Royal Society of London. Series A*, 239(1216):113–133.

Rasmussen, S. O., Abbott, P. M., Blunier, T., Bourne, A. J., Brook, E., Buchardt, S. L., Buizert, C., Chappellaz, J., Clausen, H. B., Cook, E., Dahl-Jensen, D., Davies, S. M., Guillevic, M., Kipfstuhl, S., Laepple, T., Seierstad, I. K., Severinghaus, J. P., Steffensen, J. P., Stowasser, C., Svensson, A., Vallelonga, P., Vinther, B. M., Wilhelms, F., and Winstrup, M. (2013). A first chronology for the North Greenland Eemian Ice Drilling (NEEM) ice core. *Climate of the Past*, 9:2713–2730.

Riverman, K. (2018). Enhanced firn densification in high-accumulation shear margins of the NE Greenland ice stream. Data set. Accessedon 30.03.2020.

Riverman, K. L., Alley, R. B., Anandakrishnan, S., Christianson, K., Holschuh, N. D., Medley, B., Muto, A., and Peters, L. E. (2019). Enhanced firn densification in high-accumulation shear margins of the NE Greenland ice stream. *Journal of Geophysical Research: Earth Surface*, 124:365–382.

Robin, G. d. Q. (1958). *Glaciology III: Seismic shooting and related investigations*, volume 5 of *Norwegian-British-Swedish Antarctic Expedition, 1949-52: Scientific results*. Norsk Polarinstitutt.

Salamatin, A. N., Lipenkov, V. Y., and Duval, P. (1997). Bubbly-ice densification in ice sheets: I. Theory. *Journal of Glaciology*, 43(145):387–396.

Schaller, C. F., Freitag, J., Kipfstuhl, S., Laepple, T., Steen-Larsen, H. C., and Eisen, O. (2016). A representative density profile of the North Greenland snowpack. *The Cryosphere*, 10(5):1991–2002.

Schwander, J., Sowers, T., Barnola, J.-M., Blunier, T., Fuchs, A., and Malaizé, B. (1997). Age scale of the air in the summit ice: Implication for glacial-interglacial temperature change. *Journal of Geophysical Research*, 102(D16):19483–19493.

Schwerdtfeger, P. (1963). Theoretical derivation of the thermal conductivity and diffusivity of snow. *International Association of Scientific Hydrology Publication*, 61:75–81.

Simonsen, S. B., Stenseng, L., Aðalgeirsdóttir, G., Fausto, R. S., Hvidberg, C. S., and Lucas-Picher, P. (2013). Assessing a multilayered dynamic firn-compaction model for Greenland with ASIRAS radar measurements. *Journal of Glaciology*, 59(215):545–558.

Stevens, C., D., W. E., Conway, H., and Koutnik, M. (2018). *Investigations of physical processes in polar firn through modeling and field measurements*. PhD thesis, University of Washington.

Stevens, C. M., Verjans, V., Lundin, J. M. D., Kahle, E. C., Horlings, A. N., Horlings, B. I., and Waddington, E. D. (2020). The Community Firn Model (CFM) v1.0. *Geoscientific Model Development Discussions*, 2020. In review.

Vallelonga, P., Christianson, K., Alley, R. B., Anandakrishnan, S., Christian, J. E. M., Dahl-Jensen, D., Gkinis, V., Holme, C., Jacobel, R. W., Karlsson, N. B., Keisling, B. A., Kipfstuhl, S., Kjær, H. A., Kristensen, M. E. L., Muto, A., Peters, L. E., Popp, T., Riverman, K. L., Svensson, A. M., Tibuleac, C., Vinther, B. M., Weng, Y., and Winstrup, M. (2014). Initial results from geophysical surveys and shallow coring of the Northeast Greenland ice stream (NEGIS). *The Cryosphere*, 8:1275–1287.

van der Veen, C. J. (2013). *Fundamentals of Glacier Dynamics*. CRC Press, Boca Raton, Fla., 2nd edition.

Vionnet, V., Brun, E., Morin, S., Boone, A., Faroux, S., Moigne, P. L., Martin, E., and Willemet, J.-M. (2012). The detailed snowpack scheme Crocus and its implementation in SURFEX v7.2. *Geoscientific Model Development*, 5:773–791.

Wilkinson, D. (1988). A pressure-sintering model for the densification of polar firn and glacier ice. *Journal of Glaciology*, 34(116):40–45.

Yen, Y.-C. (1981). Review of thermal properties of snow, ice, and sea ice. Technical Report Report 81-10, Cold Regions Research and Engineering Laboratory.

List of acronyms

AIS Antarctic Ice Sheet

BCO Bubble Close-Off

CFM Community Firn Model

DIP Depth-Integrated Porosity

EGRIP East Greenland Ice-Core Project

GrIS Greenland Ice Sheet

NEGIS North-East Greenland Ice Stream

RCM Regional Climate Model

List of figures